Nano-electrochemistry & Nano-photochemistry
https://www.sciltp.com/journals/nenp

Review

Rational Design of Photocatalysts for CO_2 Reduction to Multi-Carbon Products

Zhizhen Yin [1,4], Huanhuan Sun [2], Wen Li [3], Xiaoyang Liu [3], Yanxi Hu [1], Yuting Wang [1] and Gancheng Zuo [3,*]

[1] State Key Laboratory of Water Pollution Control and Green Resource Recycling, School of the Environment, Nanjing University, Nanjing 210023, China
[2] State Key Laboratory of Analytical Chemistry for Life Science, School of Chemistry and Chemical Engineering, Nanjing University, Nanjing 210023, China
[3] Jiangsu Engineering Lab of Water and Soil Eco-Remediation, School of Environment, Nanjing Normal University, Nanjing 210023, China
[4] School of Resources and Environment, Yili Normal University, Yining 835000, China
* Correspondence: zuogc@njnu.edu.cn

How To Cite: Yin, Z.; Sun, H.; Li, W.; et al. Rational Design of Photocatalysts for CO_2 Reduction to Multi-Carbon Products. *Nano-electrochemistry & Nano-photochemistry* **2025**, *1*(1), 6. https://doi.org/10.53941/nenp.2025.100006

Received: 3 October 2025
Revised: 17 November 2025
Accepted: 20 November 2025
Published: 27 November 2025

Abstract: Photocatalytic reduction of CO_2 into multi-carbon (C_{2+}) products is a promising but challenging pathway for carbon recycling, primarily hindered by the high kinetic barrier of C–C coupling and inefficient charge dynamics. This review systematically elaborates on the recent advances in photocatalyst development, focusing on key material systems including metal oxides, sulfides, Cu-based materials, graphitic carbon nitride, metal organic frameworks, and covalent-organic frameworks. It highlights the structure-activity relationships within these materials that govern the reaction pathway and selectivity. Furthermore, a systematic evaluation of performance-enhancing strategies, including defect engineering, doping engineering, heterojunction construction, and plasmonic effects, highlights their ability to precisely modulate electronic structures and reaction microenvironments, thereby promoting efficient C–C coupling. Finally, this review provides a critical discussion of current limitations and future research frontiers, offering perspectives on product verification, in-situ mechanistic studies, bifunctional synergy, and reactor design for practical application.

Keywords: photocatalyst design; photocatalytic CO_2 reduction; multi-carbon products; structure-activity relationship; reaction pathway

1. Introduction

Since the Industrial Revolution, atmospheric CO_2 concentration has risen sharply from approximately 275 ppm to over 400 ppm, significantly surpassing the natural range of 180–300 ppm observed over the past 8.0×10^5 years, with an average annual growth rate exceeding 2 ppm. This sharp increase stems from the fact that CO_2 emissions from human activities significantly outpace the natural absorption capacity, thereby leading to a range of serious ecological problems [1,2].

Against this backdrop, the conversion of CO_2 into high-value-added chemicals via photocatalytic technology is considered not only a crucial pathway for mitigating the greenhouse effect but also a promising strategy for achieving carbon resource recycling and sustainable development [3–5]. Among various CO_2 conversion technologies, photocatalytic approaches have attracted widespread attention due to their mild reaction conditions, direct utilization of solar energy, and simple reactor configurations [6]. Most importantly, this technology enables the synthesis of chemical fuels using only water and CO_2 as feedstocks, thereby avoiding byproduct pollution and representing a highly promising green synthesis route [7]. Of particular interest is the reduction of CO_2 to C_{2+}

products, such as ethylene (C_2H_4) [8], ethanol (C_2H_5OH) [9], acetic acid (C_3H_7OH) [10], acetate [11], propane(C_3H_8) [12], propionic acid (C_2H_5COOH) [13,14], propanol (C_3H_8O) [15], propylene (C_3H_6) [16], and butanol (C_4H_9OH) [17]. These compounds exhibit higher energy density, broader application prospects, and greater economic value, making them a current research hotspot. However, photocatalytic CO_2 reduction still faces several challenges, including the inherent stability of CO_2 molecules (with a C=O bond dissociation energy as high as 750 kJ·mol^{-1}) [17–21], sluggish multi-electron transfer kinetics [22], thermodynamic competition with the hydrogen evolution reaction (HER) [23–26], and difficulties in controlling product selectivity [27,28]. In particular, the efficiency of C_{2+} product formation remains considerably lower than that of C_1 products, a limitation that severely restricts the practical application of C_{2+} compounds.

The performance of the photocatalyst itself remains a core factor determining the reaction rate. In recent years, researchers have devoted efforts to developing various types of semiconductor photocatalytic materials. Some reviews have already provided detailed summaries of materials such as g-C_3N_4 [29], MOF-based materials [30–32], COF-based materials [33,34], Bi_2WO_6 [35], perovskite [36], and copper-based nanomaterials [37,38]. Meanwhile, many new strategies have been proposed for the design of high-performance photocatalysts [22,39–41]. Several systematic reviews have advanced our understanding of this field from complementary perspectives. These include summaries of material classes and dual-active sites [42], analyses of factors influencing C_{2+} selectivity [43], insights into active-site design [44], detailed mechanistic explorations [45], and emphasis on the impact of active-site structure on intermediate selectivity [46]. Figure 1 summarizes these key material categories and pivotal review perspectives, providing an overview of the research landscape in photocatalytic CO_2 reduction to C_{2+} products.

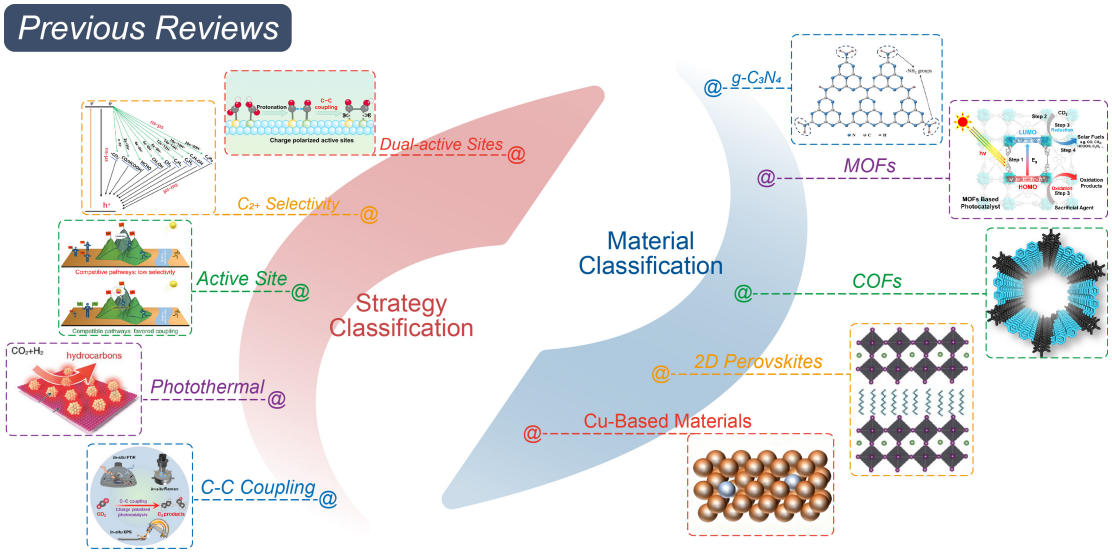

Figure 1. The research landscape of photocatalytic CO_2 reduction into C_{2+} products. Reprinted with permission from Ref. [29]. Copyright 2024, John Wiley and Sons. Reprinted with permission from Ref. [32]. Copyright 2025, American Chemical Society. Reprinted with permission from Ref. [33]. Copyright 2025, Royal Society of Chemistry. Reprinted with permission from Ref. [35]. Copyright 2024, John Wiley and Sons. Reprinted with permission from Ref. [36]. Copyright 2025, John Wiley and Sons. Reprinted with permission from Ref. [38]. Copyright 2025, John Wiley and Sons. Reprinted with permission from Ref. [42]. Copyright 2024, Royal Society of Chemistry. Reprinted with permission from Ref. [43]. Copyright 2024, Royal Society of Chemistry. Reprinted with permission from Ref. [44]. Copyright 2025, John Wiley and Sons. Reprinted with permission from Ref. [45]. Copyright 2018, John Wiley and Sons. Reprinted with permission from Ref. [46]. Copyright 2023, American Chemical Society.

While significant progress has been made, a systematic understanding of the atomic- and molecular-level mechanisms that promote C–C coupling during photocatalytic CO_2 reduction remains limited. Key aspects such as electronic structure modulation and the optimization of critical intermediate adsorption energies have yet to be fully elucidated. To bridge this knowledge gap, this review focuses on the C–C coupling enhancement mechanisms across major catalyst systems, including metal oxides, sulfides, Cu-based materials, g-C_3N_4, MOFs, and COFs. It provides a comprehensive analysis of how various strategies–such as defect engineering, doping, atomic-scale structural control, heterojunction design, plasmonic effects, dual-active-site configuration, and the integration of photothermal, photoelectrochemical, and photobiological processes–collectively enhance the efficiency and selectivity of C_{2+} product formation.

2. Challenges in Photocatalytic CO_2 Reduction into C_{2+} Products

Photocatalytic CO_2 reduction represents a promising technology that utilizes semiconductor materials to harness solar energy for converting CO_2 into hydrocarbon fuels through a series of photophysical and surface chemical processes, offering a sustainable pathway toward closing the carbon cycle (Figure 2). The mechanism initiates when a semiconductor absorbs photons with energy equal to or greater than its bandgap, exciting electrons from the valence band (VB) to the conduction band (CB), thereby generating electron-hole pairs, that is, photogenerated carriers [47,48]. A critical challenge arises from the fact that the recombination rate of these carriers, occurring on picosecond to nanosecond timescales, far exceeds the millisecond scale duration required for catalytic reactions. Thus, effective separation and migration of carriers to the catalyst surface are essential to improve quantum efficiency [49–51]. Once migrated, electrons and holes drive the reduction of CO_2 and oxidation of water, respectively [27,52]. However, CO_2 reduction faces significant selectivity challenges due to the closely spaced redox potentials of various possible products, approximately −0.7 V to −0.2 V vs. NHE at pH = 7, often resulting in mixed products that are difficult to separate [33,53]. Moreover, the conduction band minimum (CBM) must be more negative than the CO_2 reduction potential to provide adequate thermodynamic driving force, while the valence band maximum (VBM) must be more positive than the water oxidation potential to sustain the reaction cycle [53–55].

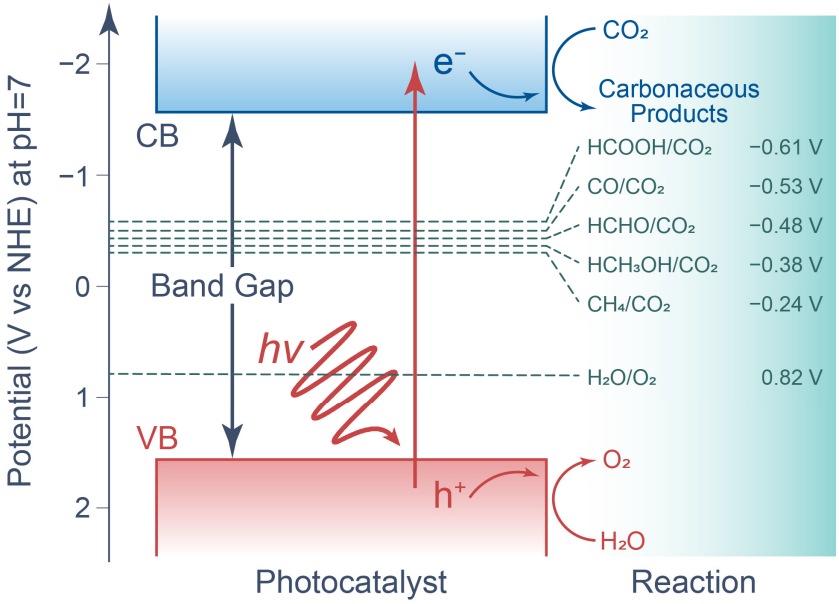

Figure 2. Schematic illustration of photocatalytic CO_2 reduction on the photocatalyst.

Building upon these fundamental constraints, the practical application of photocatalytic CO_2 reduction is further impeded by several severe challenges that critically limit the selective formation of multi-carbon products. The primary issue lies in unfavorable kinetic competition: the hydrogen evolution reaction (HER), as a dominant side reaction, significantly limits CO_2 reduction efficiency due to its thermodynamic and kinetic advantages [33,56]. Another major challenge involves the oxidation half reaction and the resulting reaction environment: the slow kinetics of the four-electron water oxidation process, coupled with the accumulation of highly oxidizing species, often compels the use of sacrificial agents. While this enhances reduction efficiency, it compromises sustainability and may lead to overestimated product yields [33]. Furthermore, the dependency of many high-performance systems on noble-metal components substantially increases material costs and restricts scalability [33]. Finally, the structural stability of catalysts under operational conditions remains a critical constraint, as degradation or decomposition can occur.

From a reaction pathway perspective, the selective synthesis of C_{2+} products constitutes one of the most demanding challenges, imposing requirements far beyond those for C_1 products. The initial single-electron reduction of CO_2 to form the CO_2^- radical requires a highly negative potential, approximately −1.90 V versus NHE at pH = 7, making it a kinetic bottleneck [57,58]. Although this barrier can be circumvented via proton-coupled electron transfer (PCET) mechanisms [59,60], the subsequent C–C coupling step introduces even slower kinetics. Generating C_{2+} products involves a complex sequence of 12 to 18 electron-proton transfers through multiple possible pathways (Figure 3), such as $*CH_3$ coupling, *CO–*CHO coupling, and others [61]. The efficiency and selectivity of these pathways are highly sensitive to the adsorption behavior of intermediates on the catalyst

surface. This imposes dual requirements on the catalyst: it must not only concentrate a high density of photogenerated electrons to sustain multi-electron reactions but also provide well-defined active sites that optimize the adsorption and activation of key intermediates [42,62].

Therefore, the fundamental challenge lies in designing catalytic materials that simultaneously address thermodynamic, kinetic, and selectivity constraints to enable efficient and selective CO_2 to C_{2+} conversion. In summary, this section has outlined the specific challenges in generating multi-carbon products, which stem from the demanding C–C coupling step, the complex multi-electron/proton transfer pathways, and the dual requirement for high electron density and well-defined active sites.

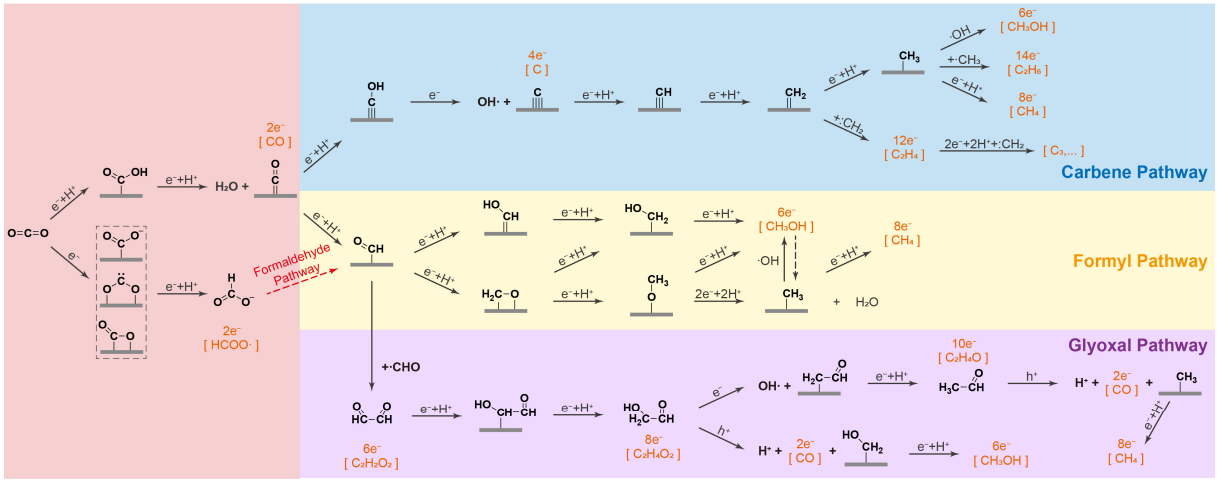

Figure 3. Mechanistic pathways of CO_2 reduction to commonly observed C_1 and C_{2+} products. Reprinted with permission from Ref. [2]. Copyright 2022, American Chemical Society.

3. A Catalyst for the Photocatalytic Reduction of CO_2 to C_{2+} Products

3.1. Metal Oxides

Metal oxides represent a pivotal class of materials for the photocatalytic reduction of CO_2 to C_{2+} products. They are conventionally categorized into three types based on their electronic configurations: d^0 type metal oxides, for example, those containing Ti^{4+}, Mo^{6+}, Ta^{5+}, Zr^{4+}, W^{6+}, Nb^{5+}; d^{10} type metal oxides, such as those incorporating Sn^{4+}, Ga^{3+}, In^{3+}, Sb^{5+}, Ge^{4+}, Cu^{+}, Zn^{2+}, and f^0 type metal oxides, including those with Ce^{4+}. Among them, d^0 type oxides have shown particular promise by stabilizing the key multi-carbon transition state through their empty d-orbitals, which is crucial for the challenging C–C coupling step.

A widely adopted strategy to lower the kinetic barrier for C–C coupling in d^0 type systems involves constructing composite structures with metal nanoparticles to create charge-asymmetric active sites. A representative example is the work by Ding et al., who engineered an interface with asymmetric charge density by depositing palladium nanoparticles onto Nb_2O_5 nanosheets (Figure 4a). The resulting structure was characterized by transmission electron microscopy (TEM, Figure 4b), which confirmed the nanosheet morphology and the presence of Pd nanoparticles, as evidenced by lattice fringes of 0.224 nm corresponding to the Pd(111) plane [63]. The interfacial electron transfer creates charge-asymmetric Pd–Nb sites, which are pivotal for C–C coupling. The resulting charge imbalance stabilizes key multi-carbon intermediates by mitigating their dipole–dipole repulsion, thereby lowering the coupling energy barrier to 1.02 eV and steering the pathway toward C_2 products.

Beyond conventional metal oxides, high entropy oxides (HEOs) have emerged as a novel material platform. HEOs are solid solutions comprising five or more principal metal cations in near equimolar ratios (5% to 35%), stabilized within a single crystal structure by high configurational entropy [64,65]. The inherent lattice distortion and complex chemical environment in HEOs create a distribution of localized electronic states that trap photogenerated electrons, prolonging charge carrier lifetime. This, combined with the synergistic effect of multiple adjacent metal cations, stabilizes the multiple *CO intermediates required for C–C coupling, although the precise mechanism demands future exploration. This innovative multi-component strategy effectively overcomes the limitations of traditional single principal component materials, thereby demonstrating remarkable adaptability across diverse catalytic applications, including thermal catalysis, photocatalysis, and electrocatalysis. Although most current studies focus on C_1 products, the considerable potential of HEOs for the selective generation of C_{2+} compounds warrants more in-depth investigation.

Shifting focus to d^{10} type systems, In^{3+}-based oxides, alongside Cu based materials, have garnered significant attention for photocatalytic CO_2 reduction to C_{2+} products. For instance, constructing an internal electric field in GDY/In_2O_3 facilitates charge separation [66], forming TiO_2/In_2O_3 heterojunctions enhances the reaction driving force [67], and incorporating reduced graphene oxide into In_2S_3/In_2O_3 establishes additional electron transport channels [68]. These strategies collectively promote the critical C–C coupling step by enriching the electron density at active sites.

Zn^{2+}-based d^{10} oxides represent another promising candidate. For example, Du et al. shifted the primary photoreduction product from CO to C_2H_4 by modifying ZnO with Pd [69]. However, most metal oxide photocatalysts are constrained by their single active sites, typically facilitating CO_2 reduction only to C_1 products. To address this limitation, researchers have proposed the design of metal oxide photocatalysts featuring charge-polarized dual active sites.

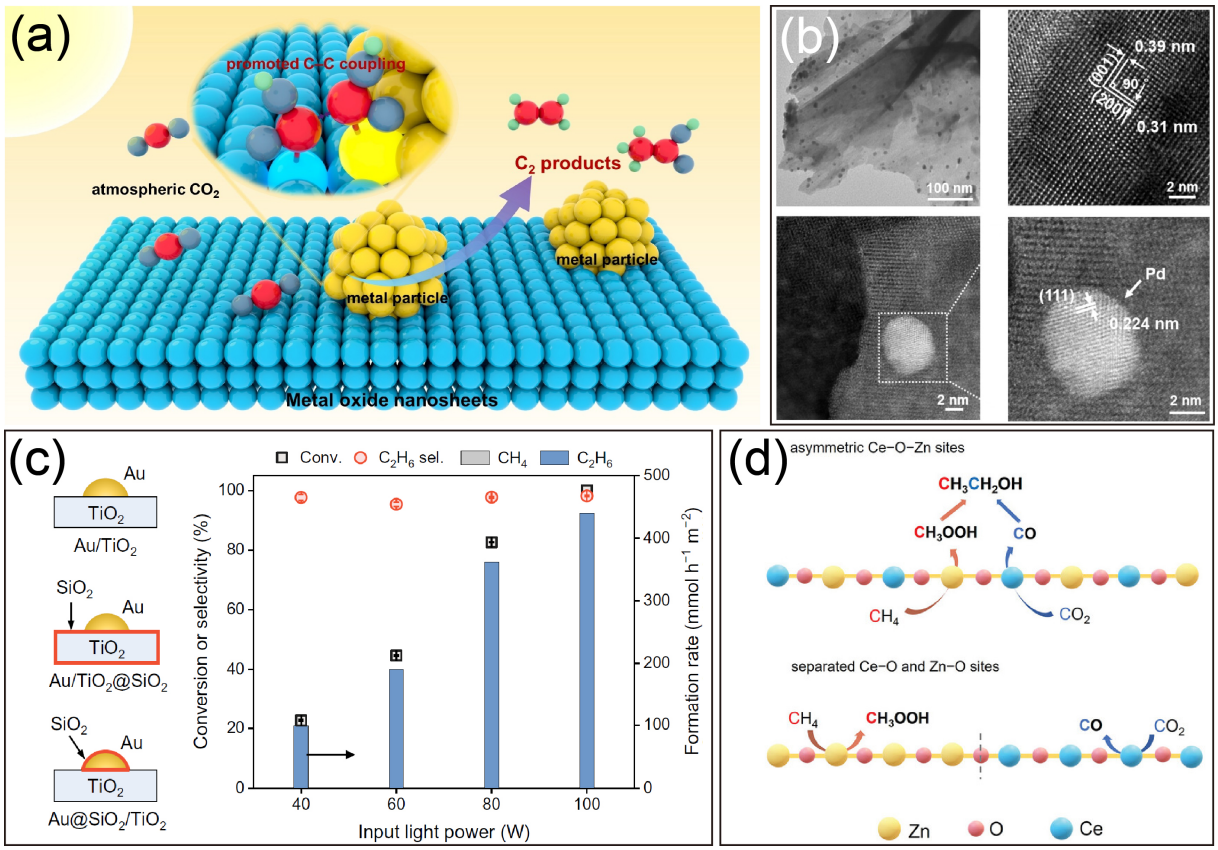

Figure 4. Photocatalytic CO_2 reduction with metal oxides. (**a**) Schematic illustration for the photoreduction of CO_2 on metal oxide nanosheets. (**b**) TEM images of Pd-Nb_2O_5. Reprinted with permission from Ref. [63]. Copyright 2025, John Wiley and Sons. Photoreduction of CO_2 with (**c**) Au@SiO_2/TiO_2 and (**d**) Ce-doped ZnO. Reprinted with permission from Ref. [8]. Copyright 2025 American Association for the Advancement of Science. Reprinted with permission from Ref. [70]. Copyright 2024, John Wiley and Sons.

A particularly notable advancement was made by Jin et al., who introduced a "photo-generated interface electric dipole" to replace conventional thermally driven Lewis acid-base designs. Using Au/TiO_2 as a model catalyst, they observed a significant, light-intensity-dependent increase in the H/D exchange rate under illumination, confirming a charge-driven hydrogen dissociation process. The finding that SiO_2 layer thickness dictates both H_2 dissociation and methanol dehydrogenation activity further pinpointed the interface as the active center (Figure 4c). This mechanism promotes $H^{\delta-}$ formation, which aids $HCOO^-$ generation and subsequent coupling with *CH_3, effectively suppressing C_1 by-products [8]. For f^0 metal oxides, the directional construction of asymmetric structures is also an effective strategy for creating dual active sites. For instance, Hao et al. developed a Ce-doped ZnO nanocomposite. The abundant asymmetric Ce-O-Zn structures in this material serve as efficient sites for the direct photocatalytic coupling of CH_4 and CO_2 to synthesize ethanol. Within this structure, the Zn-O site adsorbs and oxidizes CH_4 to form *CH_3OOH, while the adjacent Ce-O site promotes CO_2 reduction to *CO. The spatial proximity of these sites enables efficient C–C coupling of the intermediates, selectively

generating C_2H_5OH. This outcome starkly contrasts with the scenario where only C_1 products form at separated sites (Figure 4d) [70].

The nature of the catalyst support exerts a significant influence on product selectivity. Conventional C_1 selective materials, including TiO_2, ZnO, and Bi_2WO_6, remain in the exploratory phase concerning C_{2+} product generation. Studies indicate that metal oxide/metal composites (e.g., TiO_2/Pd, CuO/ZnO, Li_2O/TiO_2) exhibit moderate selectivity for C_1–C_3 compounds when supported on basic oxides such as MgO, Al_2O_3, or SiO_2. Catalysts supported on acidic oxides tend to yield C_1 compounds [71]. Beyond the support effect, the intrinsic properties of the metal oxide itself are crucial. However, systematic studies on many promising materials are still lacking. Research on CO_2 reduction using binary d^0 oxides like ZrO_2, Nb_2O_5, and Ta_2O_5 remains relatively scarce. Although d^0 type perovskites (e.g., $SrTiO_3$, $NaNbO_3$, $KTaO_3$) exhibit high stability and efficient charge separation, and d^{10} type mixed oxides (e.g., Zn_2GeO_4, Ga_2O_3, $In_2Ge_2O_7$) promote charge transfer and reactant intercalation, systematic investigation into their application for photocatalytic CO_2 reduction to C_{2+} products has not been systematically investigated.

3.2. Metal Sulfides

Metal sulfides are promising photocatalysts due to their excellent light absorption capacity and strong reducing power. These advantageous properties are attributed to their electronic structure, specifically the valence bands dominated by S 3p orbitals. This configuration typically leads to a high conduction band minimum and a narrow band gap, which collectively enhance hole mobility and improve charge separation efficiency [42,72]. More importantly for C–C coupling, the presence of charge-asymmetric metal sites in certain sulfides is particularly crucial for CO_2 reduction to C_{2+} products. Such asymmetry strengthens the adsorption of *CO intermediates and facilitates their dimerization by modulating the local electron density, thereby promoting the critical C–C coupling step [42]. A wide range of metal sulfides has been explored for photocatalytic CO_2 reduction to C_{2+} products, including disulfides such as ZnS [73], CdS [74], MoS_2 [10,75], SnS_2 [76], CuS [77], Bi_2S_3 [78], and In_2S_3 [69]; ternary sulfides such as $ZnIn_2S_4$ [79] and $CuIn_{11}S_{17}$ [80]; and polysulfides such as $Cu_2M_iM_jS_4$ (M_i = Mn, Co, Ni, Zn; M_j = Sn) [65].

Among the diverse metal sulfides, $ZnIn_2S_4$ (ZIS), a ternary sulfide with a layered structure, demonstrates considerable potential in photocatalysis and has attracted widespread research interest alongside copper-based sulfides [79]. For instance, doping ZIS with large-radius rare-earth elements (Er) creates zinc vacancies (V_{Zn}). The synergy between Er and VZn establishes a charge-asymmetric pair, where DFT calculations confirm electron transfer from VZn to Er, enhancing the built-in electric field. This field directs charge separation, while the VZn sites concurrently act as hole traps, as evidenced by fs-TAS, collectively opening efficient migration channels for markedly improved charge separation [81].

Beyond elemental doping, novel structural designs have proven highly effective. Chen et al. constructed an active structure (Au_n/Au_1–CMS) where gold single atoms coexist with nanoparticles on edge-enriched cracked MoS_2 (CMS). HRTEM images (Figure 5a) revealed lattice fringes of 0.63 nm and 0.23 nm, corresponding to the MoS_2 (002) and Au (111) planes, respectively, indicating successful Au deposition. Atomic-resolution HAADF-STEM analysis (Figure 5b) further confirmed the coexistence of isolated Au single atoms and nanoparticles on the support. This design enables exceptional selectivity for CH_3COOH (Figure 5c) by establishing a synergistic charge transfer pathway and creating Mo-Au dual sites. The electronic synergy at these sites, through Au 5d and Mo 4d orbital coupling, efficiently stabilizes the key *CH_2CO intermediate and drives the C–C coupling step, which is the origin of the high C_2 product selectivity [10]. Similarly, constructing chemical bonding interfaces serves as another powerful strategy for regulating reaction pathways. Song et al. constructed an S vacancy-rich MoS_x/Fe_2O_3 heterojunction to form Fe–S bonds, which optimized charge separation. As a result, C_2H_4 emerged as the primary product, underscoring the crucial role of *CO intermediates in the reaction (Figure 5d) [82].

A key challenge for sulfide-based photocatalysts is photocorrosion. This issue stems from the electronic structure of sulfides: their valence band, formed by S 3p orbitals, readily localizes photogenerated holes on S^{2-} sites, leading to oxidative dissolution. Mitigating this requires engineering charge transfer pathways to divert holes away from the lattice. For instance, forming a heterojunction can create a driving force for hole extraction, while introducing sulfur vacancies can serve as hole traps, both stabilizing the structure against degradation [83,84]. Overall, the exploration of sulfide materials for selective C_{2+} production is still in its early stages, with many systems beyond the most prominent examples remaining underexplored and warranting further investigation.

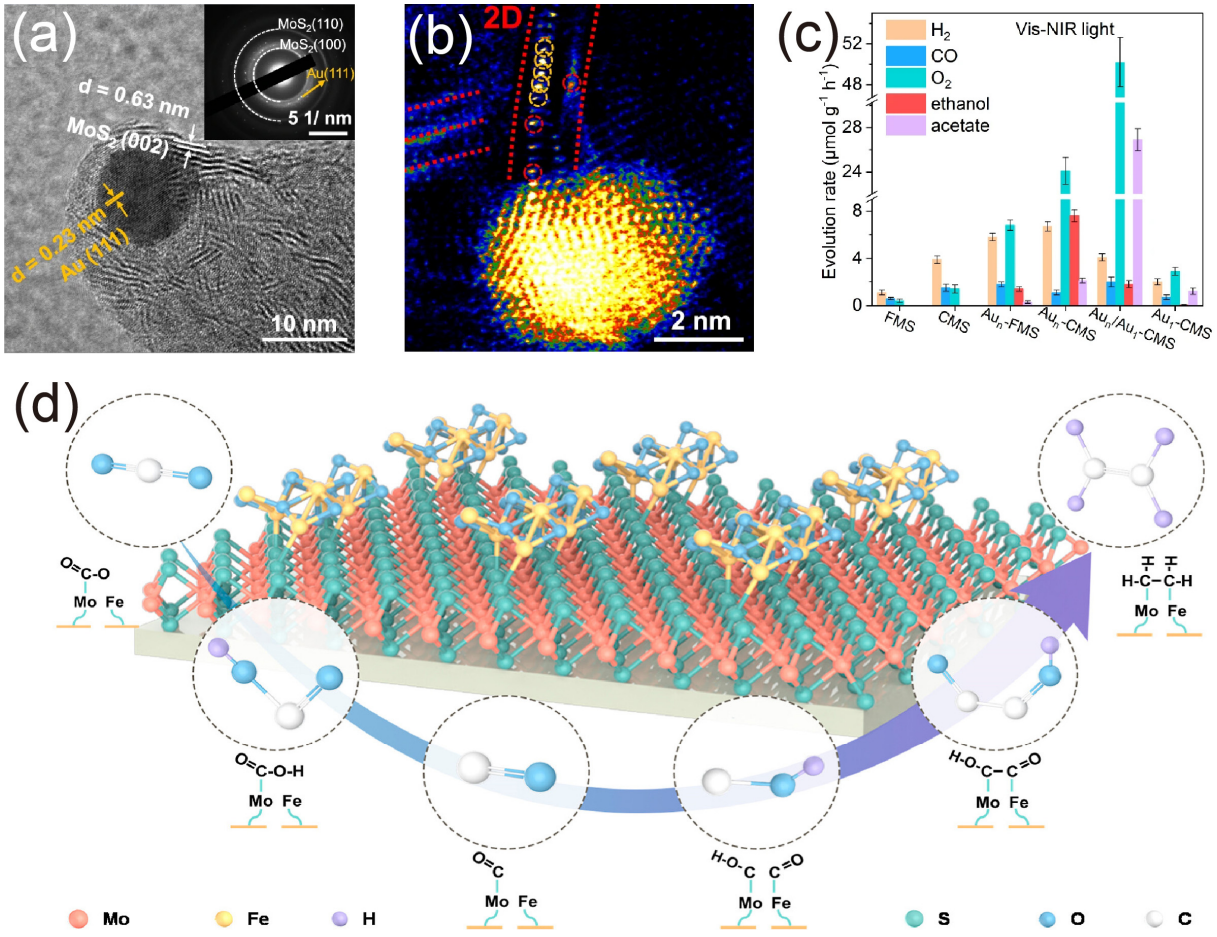

Figure 5. Photocatalytic CO_2 reduction with metal sulfides. (**a**) HRTEM image; (**b**) HAADF-STEM image; and (**c**) performance of Au_n/Au_1–CMS. Reprinted with permission from Ref. [10]. Copyright 2024, Springer Nature. (**d**) Schematic illustration of photocatalytic CO_2 reduction to ethylene over the MoS_x/Fe_2O_3 photocatalyst sheet. Reprinted with permission from Ref. [82]. Copyright 2024, American Chemical Society.

3.3. Cu-Based Materials

Copper-based materials are primary candidate catalysts for converting CO_2 to C_{2+} products, owing to their earth abundance and unique capability to activate C–C coupling via moderate *CO adsorption and subsequent dimerization [81]. Based on recent advances in Cu-based catalysts, this section reviews the research status and mechanisms of two material categories: small-sized copper species stabilized on inorganic supports and copper-based compounds.

For small-sized copper species, the focus lies on the rational design of the local coordination and electronic structure of active sites to precisely steer the catalytic pathway. Cu single-atom catalysts (SACs), with their atomically dispersed and highly tunable sites, have enabled the optimization of CO_2 adsorption, C–C coupling, and intermediate stabilization through strategies such as coordination number adjustment, dual site synergy, and defect engineering, thereby facilitating the efficient and selective synthesis of multi-carbon products. For example, Shen et al. constructed monolayer $Ti_{0.91}O_2$ nanosheets (~0.85 nm thick) implanted with single Cu atoms to prepare a Cu–Ti–V_O/$Ti_{0.91}O_2$–SL catalyst. Charge density analysis indicated a transfer of 0.3 e^- from Ti to Cu, creating an asymmetric electron distribution at the Cu–Ti sites, in contrast to the localized electron density observed in the V_O-free sample (Figure 6a). Photocatalytic performance evaluation showed that Cu–Ti–V_O/$Ti_{0.91}O_2$–SL achieved C_2H_4 and C_3H_8 yields of 7.6 and 13.8 μmol·g^{-1}·h^{-1}, respectively, along with 18.6 μmol·g^{-1}·h^{-1} of CO (Figure 6b), underscoring its significantly enhanced C–C coupling capability compared to other catalysts [12]. In another approach, Yang et al. utilized an interlayer stacking effect to construct a supramolecular catalyst (HCDS) via Cu^{2+} coordination self-assembly, also aiming to promote C–C coupling by regulating the active site microenvironment. The unique directional electron migration channels in this catalyst can efficiently enrich photogenerated electrons at the copper active centers. The uniformly distributed sites effectively enhance the selectivity toward C–C coupling by suppressing competing pathways, thereby steering the reaction toward C_{2+} products [22].

Copper-based compounds, particularly sulfides and oxides, have demonstrated significant potential in the photocatalytic reduction of CO_2 to C_{2+} products. Current research focuses on optimizing the adsorption strength and surface coverage of *CO intermediates on copper-based sulfides by tailoring their local coordination environment, for instance, through the creation of sulfur vacancies, the formation of heterojunctions, or the fabrication of atomically dispersed active sites, thereby facilitating C–C coupling to generate C_{2+} products.

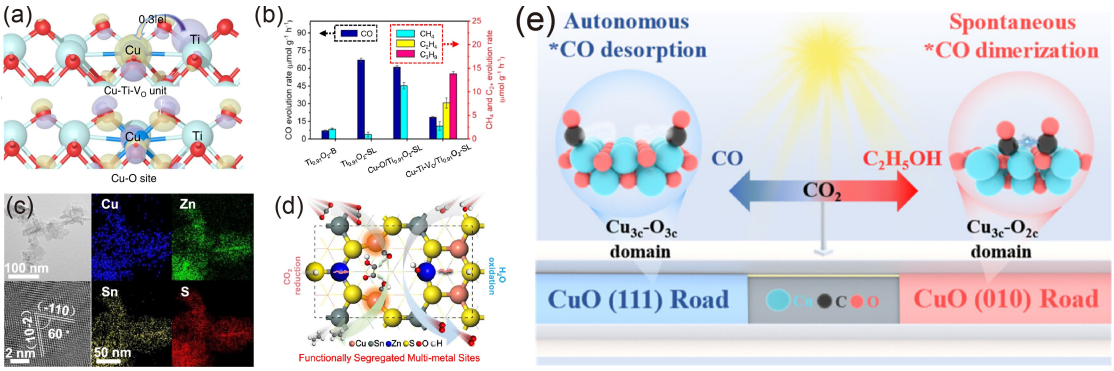

Figure 6. Cu-based materials for photocatalytic CO_2 reduction. (**a**) Charge density differences and (**b**) product rates of Cu-Ti-VO/$Ti_{0.91}O_2$. Reprinted with permission from Ref. [12]. Copyright 2023, Springer Nature. (**c**) HRTEM images and (**d**) photocatalytic mechanism of Cu_2ZnSnS_4. Reprinted with permission from Ref. [65]. Copyright 2025, Springer Nature. (**e**) Selective photocatalytic conversion of CO_2 with CuO. Reprinted with permission from Ref. [85]. Copyright 2024, American Chemical Society.

In Cu-based sulfides, electronic structure modulation is a key strategy. Li et al. developed a multi-site catalyst, implementing a strategy that led to the synthesis of $Cu_2MiM_jS_4$-S_v nanosheets, as structurally verified by TEM/HRTEM (Figure 6c). This system operates via a functional synergy (Figure 6d): Cu sites, electronically tuned by Bader charge, are responsible for C–C coupling, while S sites manage proton transfer, collectively enabling high-efficiency C_2H_4 production [65]. In a related study, Shi et al. synthesized three copper single-atom catalysts with tailored coordination environments. Electronic structure analysis showed that while all three Cu catalysts introduced new electronic states near the Fermi level, the energy level of the Cu–N_2–V configuration was the closest. Electron occupation analysis further confirmed a higher electron density at this level in Cu–N_2–V. Charge density distribution also revealed pronounced charge accumulation at the Cu sites in Cu–N_2–V, in contrast to the charge depletion observed in Cu–N_3 and Cu–N_4. These distinctive electronic features collectively enhance CO_2 activation and facilitate C–C coupling, leading selectively to ethanol formation [85].

Beyond sulfides, Cu-based oxide systems also show great promise. To enhance selectivity toward multicarbon products, Wang et al. developed a dual center strategy based on coordination number regulation. The synergy between tricoordinated copper (Cu_{3c}), which boosts *CO coverage, and bicoordinated oxygen (O_{2c}), which guides *CO migration, significantly reduces the energy barrier for C–C coupling (Figure 6e) [85]. This design enables a CuO catalyst to achieve outstanding ethanol selectivity (96.9%) and stability.

Furthermore, constructing composite structures represents another effective approach to push the performance boundaries of Cu-based catalysts. For instance, CuPt/WO_3 prolonged the residence time of *CO intermediates through Cl^- coordination, achieving 88.1% selectivity toward acetic acid. Its hexagonal pore structure promotes multi-electron/proton transfer dynamics and C–C coupling [86]. Similarly, CuO_x@p-ZnO utilized porous confinement and mixed valence Cu^+/Cu^{2+} to promote *CO dimerization, achieving 32.9% ethylene selectivity with a yield of 2.7 μmol·g^{-1}·h^{-1} [61].

3.4. g-C_3N_4

g-C_3N_4, a metal-free polymer semiconductor with a medium bandgap, is widely recognized for its excellent chemical and thermal stability. The abundant amino groups (–NH_2) on its surface facilitate CO_2 adsorption, making it a promising photocatalytic material [29,87]. Its CB and VB are positioned at approximately −1.1 eV and +1.6 eV (vs. NHE), respectively. This band structure enables it to thermodynamically drive a variety of photocatalytic reactions [88,89]. However, g-C_3N_4 still suffers from limitations such as low quantum yield, small specific surface area, and rapid charge carrier recombination [87].

To overcome these limitations, extensive research has been directed toward modulating its morphology and electronic structure. Morphological engineering across different dimensions has been explored: zero dimensional quantum dots can provide abundant surface active sites [90]; one dimensional nanotubes can enhance light

harvesting through multiple scattering and reflection [91]; two dimensional nanosheets can induce quantum confinement effects at specific sizes, enhancing the redox capacity of charge carriers [87]; and three dimensional porous frameworks are beneficial for mass transfer and stability improvement [92]. Notably, the morphological and dimensional characteristics of g-C_3N_4 are key factors influencing the selectivity of photocatalytic CO_2 reduction toward C_{2+} products. Current research on C_{2+} products primarily focuses on two-dimensional g-C_3N_4 nanosheets, whereas quantum dot structures are commonly used in photothermal catalysis for generating C_1 products. For instance, a composite semiconductor constructed from 2D g-C_3N_4 and $K_2Fe_2O_4$ achieved highly selective conversion of CO_2 to hydrocarbon products without sacrificial agents [93].

Beyond morphology, precise engineering of the electronic structure is paramount for steering the reaction pathway toward C–C coupling. Chen et al. engineered g-C_3N_4 nanosheets with carbon doping and nitrogen vacancies (PCCN-10) to steer CO_2 photoreduction toward C_2H_6. Electron density difference reveal that this modification breaks the symmetric electron distribution of pristine g-C_3N_4, creating electron-rich regions that lower the energy barrier for C–C coupling (Figure 7a). Consequently, PCCN-10 achieves a high C_2H_6 production rate of 99.14 μmol·g^{-1}·h^{-1}, with only trace amounts of CO and CH_4 detected (Figure 7b), underscoring the critical role of electronic structure modulation in selective C_{2+} formation [94]. In a similar vein, Li et al. demonstrated that a dipole-limited domain field, induced by double vacancies, promotes C–C coupling by concentrating C_1 intermediates. As revealed by differential charge density analysis (Figure 7c), this field strengthens CO_2 adsorption and polarization by withdrawing electrons. This effect enables $V_{C,N}$–CN-650 to achieve a high C_2H_6 yield of 57.86 μmol·g^{-1}·h^{-1} with 59.1% selectivity (Figure 7d), highlighting its efficacy in steering the reaction toward C_{2+} products [62]. Other strategies, such as cyano modification, can modulate the spatial distribution of charges through an internal electric field, forming localized high charge density reaction sites. This enhances the adsorption and activation of CO_2 and *CO intermediates, achieving efficient conversion of CO_2 to CH_4 (6.64 μmol·g^{-1}·h^{-1}) and C_2H_4 (1.35 μmol·g^{-1}·h^{-1}), with a total hydrocarbon selectivity of 84.9% [95]. Furthermore, incorporating metal atoms into the g-C_3N_4 framework can generate charge-polarized dual sites, which can be utilized to promote C–C coupling for the production of C_{2+} products [42,96].

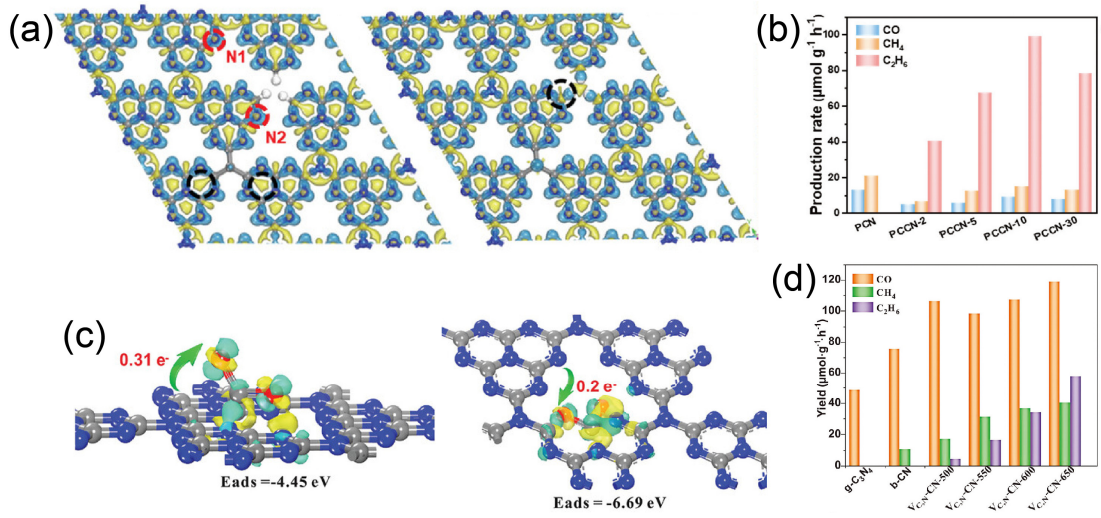

Figure 7. g-C_3N_4 for photocatalytic CO_2 reduction. (**a**) Difference in electron density of C and N for PCCN-10; (**b**) Product rates of PCCN-10. Reprinted with permission from Ref. [94]. Copyright 2025, John Wiley and Sons. (**c**) Charge density differences and (**d**) product rates of $V_{C,N}$-CN-650. Reprinted with permission from Ref. [62]. Copyright 2025, John Wiley and Sons.

In summary, research on g-C_3N_4 has evolved from leveraging its intrinsic properties to the precise engineering of its dimensionality and electronic structure. This shift in strategy, encompassing techniques such as defect introduction, doping, and the preparation of ultrathin nanostructures, aims to create a favorable local reaction environment on the catalyst surface. This microenvironment effectively enriches and stabilizes key *CO intermediates, thereby overcoming the energy barrier of C–C coupling and ultimately enabling the efficient generation of multi-carbon products.

3.5. Metal Organic Frameworks (MOFs)

MOFs are crystalline porous materials formed by the coordination-driven assembly of metal ions or clusters with organic linkers [97,98]. Owing to their designable pore structures, high specific surface areas, and well-defined active sites, MOFs exhibit unique advantages in the field of photocatalysis. However, several challenges remain in the photocatalytic conversion of CO_2 to C_{2+} products using MOFs, including: (1) Although metal cluster nodes can effectively activate CO_2 molecules and stabilize C_1 intermediates, they often struggle to drive subsequent C–C coupling to form higher-value C_{2+} products [84]; (2) The framework structure is susceptible to degradation under reaction conditions, limiting its long-term applicability [99]; (3) Mass transfer limitations within the pores and insufficient stabilization of key C_2 intermediates further inhibit reaction efficiency [100]. Based on a systematic analysis of nearly 300 publications, P. M. Stanley et al. categorize MOF synthesis strategies into node catalysis, molecular catalysis, nanoparticle catalysis, hybrid materials, and dimensionality control. This section reviews recent advances in MOFs for promoting C–C coupling and enhancing C_{2+} product selectivity within this framework [32].

Within this framework, node catalysis currently focuses heavily on copper site regulation. A representative example of this strategy is the Cu dual-site framework CuBTC-D, which was created by generating ligand defects and compounded with semiconductors to enable the efficient conversion of CO_2 to C_2H_4. This unique structure facilitates rapid electron transfer to the adjacent Cu_2 sites, promoting C–C coupling. As a result, the CuBTC-D/TiO_2 system exhibits the highest photocatalytic activity, achieving a C_2H_4 yield of 7.15 $mmol \cdot g^{-1} \cdot h^{-1}$ [101]. In another example, the g-C_3N_4/Cu-CuTCPP hybrid formed via π–π stacking allows photogenerated electrons from g-C_3N_4 to drive the reconstruction of $Cu_2(COO)_4$ nodes into $Cu_2^{1+\delta}(COO)_3$ units. This reconfiguration reduces steric hindrance, facilitating synergistic CO_2 adsorption at dual Cu sites. Concurrently, the MOF pore confinement prolongs intermediate residence time, while dissociated carboxylates act as proton relays to promote C–H formation, collectively enhancing C–C coupling and boosting C_2H_6 production [102]. These examples reveal the crucial role of MOF node sites in the photocatalytic mechanism. In the realm of nanoparticle catalysis, Chen et al. constructed a synergistic catalytic system within the MOF NU-1000 by co-loading copper single atoms and Cu doped Au nanoparticles (Figure 8). This architecture, characterized by adjacent yet functionally distinct sites, is pivotal for enabling complex multi-step reactions like C–C coupling [103].

For dimensionality control, a novel strategy leveraging the structural instability from thorium (Th) nodes' large ionic radius and high coordination number has been employed. A heat-induced multi-step crystal transformation strategy was used to precisely regulate the evolution of actinide porphyrin MOFs from IHEP-21/21(M) through IHEP-22/22(M) to IHEP-23/23(M). This process transforms the stacking of porphyrin molecules from a disordered state to a highly ordered, staggered arrangement, thereby establishing efficient electron-transfer channels and significantly enhancing photocatalytic performance [104]. Although this study focused on C1 products, it establishes a paradigm for optimizing the spatial ordering of active sites in MOFs to facilitate C-C coupling and the selective generation of C_{2+} products.

Hybrid synthesis serves as another powerful strategy to optimize the photocatalytic performance of MOFs. For example, Wang et al. *in situ* synthesized UiO-66(Zr/Ce) nanosheets on g-C_3N_4 using Zr/Ce single atoms. The composite promotes electron migration to the surface, while the interfacial built-in electric field directs photogenerated electrons to Ce sites, enhancing multi-electron reduction. The energy barrier of the rate-determining step *COOH to *CO is reduced to 0.59 eV in the composite, and the moderate H* adsorption energy optimizes hydrogenation, collectively steering the pathway toward CH_3OH, C_2H_5OH, and other liquid products. Molecular catalytic MOFs have been more extensively studied for C_1 product generation [99]. It is noteworthy that molecular catalytic MOFs have been more extensively studied for C_1 product generation.

In summary, MOF synthesis strategies, such as node catalysis, nanoparticle catalysis, hybrid synthesis, and dimensionality control, effectively reduce the energy barrier for C–C coupling and significantly promote the formation of C_{2+} products by constructing complex active sites or achieving structural ordering. This finding is highly consistent with recent research conclusions: MOF composites featuring bimetallic or charge-polarized active sites tend to selectively generate C_{2+} products when used as photocatalysts [42].

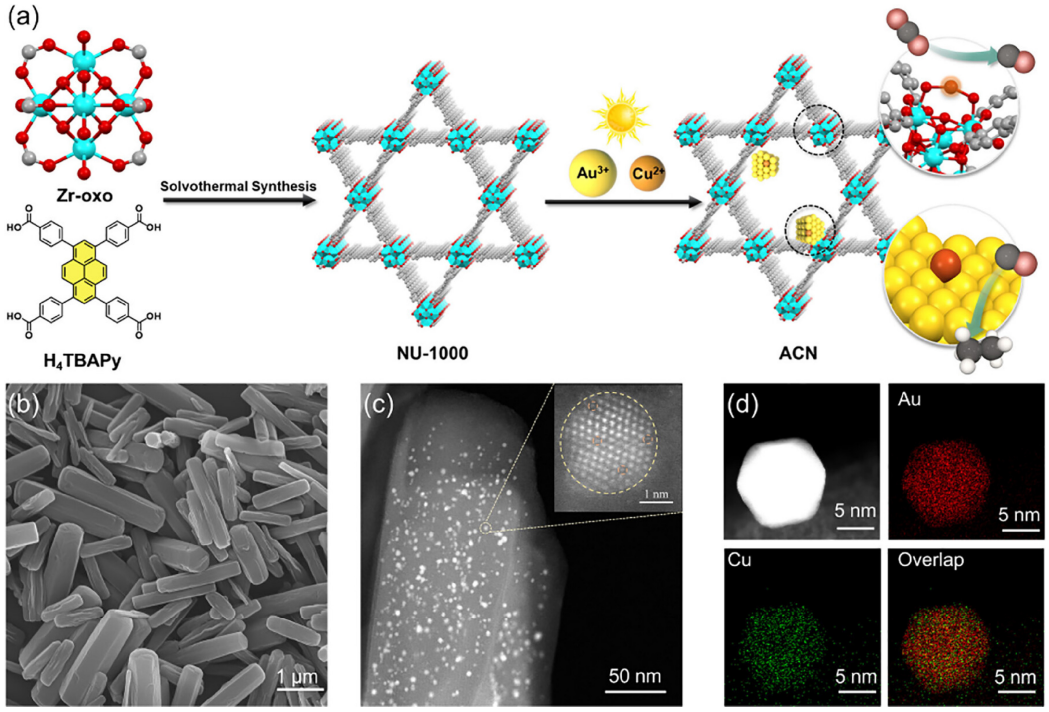

Figure 8. MOFs for photocatalytic CO_2 reduction. (**a**) Schematic illustration for the synthesis, (**b**) SEM image, (**c**) TEM image, and (**d**) elemental mappings of Cu-doped Au nanoparticles anchored on NU-1000. Reprinted with permission from Ref. [103]. Copyright 2025, American Chemical Society.

3.6. Covalent Organic Frameworks (COF)

COFs represent an important class of porous crystalline polymers for photocatalytic CO_2 reduction. They can be categorized based on different criteria. Based on their structural units, they can be classified into several categories, such as porphyrin-based, pyridine-based, and heteroaromatic-group-based COFs, which have shown promising applications in the conversion of CO_2 to C_{2+} products [105]. Alternatively, according to the presence or absence of metal sites, these materials can be divided into metal-free COFs and metal-incorporated COFs, each offering distinct advantages in photocatalytic CO_2 valorization.

3.6.1. Metal-Free COFs

Metal-free COFs primarily rely on heteroaromatic building blocks such as benzooxazole, benzothiazole, phenazine, and thiazolo [5,4-d]thiazole to achieve photocatalytic activity. These frameworks facilitate interlayer charge migration through π–π stacking, while heteroatoms (e.g., N, O, S) introduce active sites, modulate electronic structures, and form donor–acceptor (D–A) configurations, thereby narrowing the band gap and enhancing visible-light absorption [33]. The effectiveness of these design principles is clearly demonstrated in several recent studies. For example, Huang et al. elucidated the critical role of bridging motifs in COFs for photocatalysis by designing two structurally similar anthraquinone-based frameworks. The DA-COF, featuring a unique cleft-like structure and an adjacent electron donor-acceptor configuration, created an enzyme-like microenvironment that enhanced proton capture and charge migration. This strategic design resulted in a markedly higher propylene yield of 270.54 $\mu mol \cdot g^{-1}$ compared to the control DP-COF, underscoring the importance of precise structural engineering at the molecular level [16]. Figure 9 illustrates the structure and catalytic mechanism of a phenazine-based 2D COF (Phen-COF) developed by Hirani et al., which enhances the production of formate and oxalate due to the high local density of active phenazine units [106]. Additionally, triazole-based COFs (TFPB-TRZ COF) can stabilize key *CO intermediates and promote multi-electron reduction under weak basic conditions, facilitating C–C coupling [33].

The photocatalytic performance of metal-free COFs is governed not only by their molecular composition but also by their structural architecture. Structural engineering plays a vital role in enhancing their performance. Two-dimensional (2D) COFs exhibit high charge-carrier mobility and active-site accessibility due to interlayer π–π stacking and ordered pores [107]. Exfoliation into covalent organic nanosheets (CONs) or increasing the interlayer distance can further improve mass transport and catalytic efficiency [33]. Although three-dimensional (3D) COFs are less studied for CO_2 reduction, their high surface area, interconnected pores, and multidimensional charge-

transport pathways offer great potential for CO_2 adsorption and C–C coupling [108,109]. Beyond structural dimensionality, key strategies to improve metal-free COFs also include constructing D–A structures, introducing heteroatoms, fabricating rigid COF membranes, and employing nitrogen-rich linkers to stabilize reactive intermediates [33]. Additionally, to overcome inherent limitations in light absorption, exogenous photosensitizers (e.g., Ir or Ru complexes) can be incorporated to inject electrons into the COF framework [106].

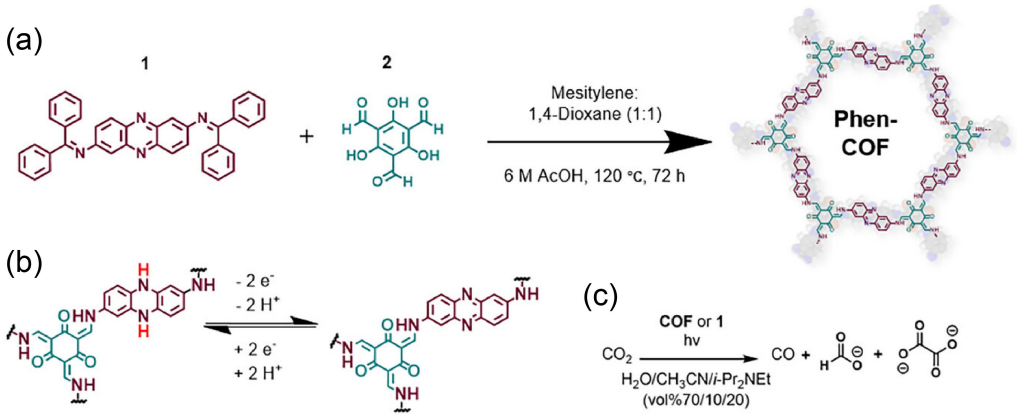

Figure 9. COFs for photocatalytic CO_2 reduction. Chemical formula of Phen-COF (**a**) synthesis, (**b**) redox activity, and (**c**) photocatalytic CO_2 reduction. Reprinted with permission from Ref. [106]. Copyright 2025, John Wiley and Sons.

3.6.2. Metal-Incorporated COFs

Metal-incorporated COFs introduce metal species either as integral components of the framework (e.g., metalloporphyrins) or through post-synthetic modification, significantly enhancing light absorption, charge separation, and catalytic specificity. Porphyrin-based COFs can coordinate with metal ions such as Zn^{2+}, Cu^{2+}, Co^{2+}, and Ni^{2+} to form well-defined active centers that improve CO_2 adsorption and direct electron transfer [110]. Although many of these systems still produce primarily C_1 products, some have demonstrated potential for C_{2+} synthesis. For instance, a cobalt-porphyrin network modified with benzothiadiazole and hydroxyl groups achieved an ethane yield of 3.7 $mol \cdot g^{-1} \cdot h^{-1}$ by optimizing charge separation [111]. Pyridine-based COFs provide nitrogen-rich platforms for anchoring metal atoms. Cu@Py-BTDA-COF, for example, contains uniformly distributed Cu pairs that facilitate C–C coupling via a local electric field, with *in situ* FTIR confirming the key CO–CO dimer intermediate [112]. Topological design is equally important for enhancing photocatalytic performance. For instance, BTA–COF–Cu, which features a kgm topology that incorporates Cu sites into a bipyridine skeleton, enables propylene production by synergistically improving light absorption and charge carrier separation [113].

3.6.3. Hybrid COF Materials

An emerging trend is the construction of hybrid materials that combine COFs with other functional materials. MOF–COF hybrids (also termed MCOFs) merge the crystallinity of MOFs with the structural tunability of COFs, creating synergistic environments for catalysis [114]. Zhang et al. developed a single-crystal MOF–COF hybrid with adjacent porphyrin units that stabilize *CO and *HCO intermediates, leading to selective ethanol production [115]. It is important to note that the term "MCOF" has also been used to denote "metal covalent organic frameworks, where metals are part of the COF skeleton, which is a distinct concept from the MOF COF hybrids discussed above. For instance, computational screening identified MgFe–S–COF and MgZn–S–COF as promising candidates for C_2H_4 production, with very low C–C coupling barriers (~0.03–0.04 eV) due to asymmetric charge distribution and a "donor acceptor antidonor" mechanism [16].

Another prominent hybrid strategy involves incorporating metal nanoclusters into COFs. To guide and utilize photogenerated electrons efficiently, bimetallic PdIn nanoclusters were confined within a photosensitizing N_3–COF to construct PdIn@N_3–COF composites. Owing to a synergistic effect that suppresses charge recombination and promotes C–C coupling, the PdIn@N_3–COF catalyst achieved a record alcohol production yield of 798 $mol \cdot g^{-1}$ [116]. Beyond compositional hybridization, microenvironmental control, such as introducing 18-crown-6 into a cobalt phthalocyanine-based COF to increase local K^+ concentration and create a localized electric field, boosted CO_2 reduction activity by 180% [117].

In summary, advances in photocatalytic CO_2 conversion to multi-carbon products using COFs are driven by sophisticated design at multiple scales. This progress hinges on molecular-level engineering of active sites in both metal-free and metal-incorporated systems, strategic control over structural dimensionality and porosity in two-

dimensional and three-dimensional frameworks, and the innovative development of hybrid materials and tailored catalytic microenvironments. Collectively, recent research demonstrates that the concerted application of these approaches, which fine-tune electronic properties, enhance mass transport, and stabilize critical reaction intermediates, is essential for guiding complex multi-electron processes toward efficient formation of desired multi-carbon compounds. The performance metrics presented in Table 1 underscore a central theme of this review: while significant progress has been made, particularly for C_{2+} products, the pursuit of catalysts that combine high yield, high selectivity, and long-term stability remains a crucial endeavor for the field.

4. Performance Improvement Strategies

4.1. Defects

Defect engineering enables the precise creation of active sites at the atomic scale, offering a powerful strategy for complex C_{2+} synthesis. Among various defect structures, point defects such as vacancies and heteroatom dopants are particularly effective for tailoring the local coordination environment of catalytic centers. This precision facilitates the construction of multi-atomic sites with specific geometries and electronic properties [118].

The construction of a triple-atomic site through defect engineering is a promising strategy for complex C_{2+} synthesis. Zhang et al. achieved this by incorporating copper into a defective MOF, forming defined CuN_2O_2 units (Figure 10a). Here, the Cu site activates CO_2 while adjacent $–NH_2$ groups cooperate to stabilize intermediates, facilitating sequential C–C coupling that yields acetone with 97% selectivity, underscoring the efficacy of atomically precise design [119]. Defects can act synergistically with surface modifications. For example, Cu nanoparticles were co-loaded with $SCN^–$ on TiO_2, where the Cu cocatalyst serves as the active site for C–C coupling and promotes carbon chain growth via the *CO–CHO intermediate pathway. The nucleophilic $SCN^–$ not only enhances CO_2 adsorption but also improves charge carrier separation and multi-electron transfer efficiency through its induced surface dipole effect [120]. Regarding the synergy between surface defects and point defects, a unique $CuIn_{11}S_{17}$ nanostructure has been designed by modulating the electronic structure microenvironment. The crystal–amorphous interface in this structure contains sulfur in different chemical states, which effectively alleviates kinetic and thermodynamic limitations. Sulfur vacancies act as H_2O adsorption sites, enhancing proton supply while reducing the energy barrier for *COOH formation [80].

Vacancy engineering serves as a powerful strategy to steer the CO_2 reduction pathway by modulating the geometric and electronic structure of active sites. In ultrathin $CuGaS_2/Ga_2S_3$, sulfur vacancies induce electron delocalization and facilitate the formation of a Cu–Ga metal-bonded bilayer (Figure 10b), leading to C_2H_4 production with a high selectivity of 93.87%. The catalytic performance is further governed by the oxidation state of Cu sites, as evidenced by a volcano-type relationship between the Cu^+/Cu^{2+} ratio and both the yield and selectivity of C_2H_4 (Figure 10b). An optimal ratio of 1 maximizes the C–C coupling efficiency by balancing the role of Cu^+ in promoting *CO dimerization and that of Cu^{2+} in stabilizing *CO adsorption [121].

It is worth noting that some scholars have further explored the thermodynamic and kinetic effects of vacancy concentration on reaction pathways. Chen et al. demonstrated that precisely tuning chalcogen vacancy concentrations in MoSSe directs photocatalytic CO_2 reduction pathways toward C_{2+} products. By creating vacancy-induced localized electronic states, they enhanced charge density and carrier migration, which lowered the energy barrier for forming key $*CH_x$ intermediates. This strategic modification lowers the energy barrier for key C_1 intermediate coupling, thereby facilitating C-C growth, as confirmed by *in situ* spectroscopy and theoretical calculations [122]. Moreover, the study by Liu et al. promoted the rapid accumulation and coupling of C_1 intermediates (*CO and *CHO) through the formation of dipole-restricted domain fields (DLDF) via C/N double vacancies. Their work first proposed a DLDF active site structure model for the photocatalytic CO_2 reduction to C_{2+} products [62]. To address the challenge of selective reaction pathways, Liu et al. constructed oxygen vacancies (O_Vs) on Bi_2WO_6 coordinated with Au–Cu dual single atoms. This design enables a clear functional division, where Cu sites activate intermediates while Au sites enrich electrons. The tailored electronic structure and accelerated charge transfer collectively enhance CO_2 adsorption and promote the formation of key carbonate intermediates, thereby achieving highly selective C_3H_6 generation alongside improved activity and selectivity toward C_{2+} products [123].

To sum up, vacancies primarily function through three main mechanisms. First, they alter the electronic and geometric structure of active sites; second, they modulate charge distribution and carrier dynamics; and third, they serve as proton-transfer stations by supplying protons and regulating reaction pathways. Beyond these roles, defects themselves can act as active sites, anchoring atomic-level species and complementing heterojunction charge separation. Practical application, however, requires careful control of defect concentration to prevent excessive charge recombination. Moreover, in catalyst design, defects play a foundational role in tailoring the reaction microenvironment, thereby enabling the integration of other strategies to collectively promote C-C coupling.

Table 1. Performance summary of representative photocatalysts for CO_2 reduction to C_{2+} products.

Catalyst	C_{2+} Products	Yield ($\mu mol \cdot g^{-1} \cdot h^{-1}$)	Product Selectivity (%)	Light Source	Light Intensity	Sacrificial Agent	CO_2 Condition	Ref.
Pd-Nb_2O_5	CH_3COOH	13.5	39.3	300 W Xe AM 1.5G	100 mW/cm^2	N/S	0.03% CO_2, 1 atm	[63]
Ce-ZnO	C_2H_5OH	580	N/S	300 W Xe	N/S	None	CO_2 (0.4 MPa) CH_4 (1 MPa)	[70]
Au_n/Au_1-CMS	CH_3COOH	26.9	86.4	300 W Xe	200 mW/cm^2	None	CO_2, 1 atm	[10]
MoS_x/Fe_2O_3	C_2H_4	10.6	84.9	300 W Xe (AM 1.5G)	100 mW/cm^2	None	CO_2, 1 atm	[82]
Cu-$Ti_{0.91}O_2$	C_2H_4 C_3H_8	7.6 13.8	17.8 32.4	300 W Xe	N/S	None	CO_2, 1 atm	[12]
HCDS	C_2H_6 C_2H_4	250.9 10	64.2 2.56	300 W Xe	N/S	Trolamine	CO_2, 0.3 atm	[22]
Cu_2ZnSnS_4	C_2H_4	25.16	63.6	300 W Xe (AM 1.5G, ≥400 nm)	50 mW/cm^2	None	CO_2, 1 atm	[65]
Cu–N_2–V	C_2H_5OH	69.8	97.8	300 W Xe	100 mW/cm^2	N/S	CO_2, 0.8 atm	[84]
CuO(010)	C_2H_5OH	30.5	96.9	300 W Xe	N/S	N/S	CO_2, 1 atm	[85]
DA-COF	C_3H_6	270.54	15.19	300 W Xe (≥420 nm)	N/S	Trolamine	CO_2,1 atm	[16]
PCCN-10	C_2H_6	99.14	80.33	300 W Xe	N/S	None	CO_2,1 atm	[94]
$V_{C,N}$–CN-650	C_2H_6	57.86	59.1	300 W Xe	N/S	None	CO_2, 1 atm	[62]
Cu-CuTCPP/g-C_3N_4	C_2H_6	18.5	44	300 W Xe (360–800 nm)	150 mW/cm^2	Triethylamine	CO_2, 1 atm	[102]
Au/Cu-NU-1000	C_2H_6	69.9	71.1	300 W Xe AM 1.5G	N/S	BIH	CO_2, 1 atm	[103]
g-C_3N_4/UiO-66(Zr/Ce)	C_2H_5OH	38.10	/	300W Xe	660 mW/cm^2	None	CO_2, 1 atm	[99]

Note: N/S stands for “Not Specified” in the original source.

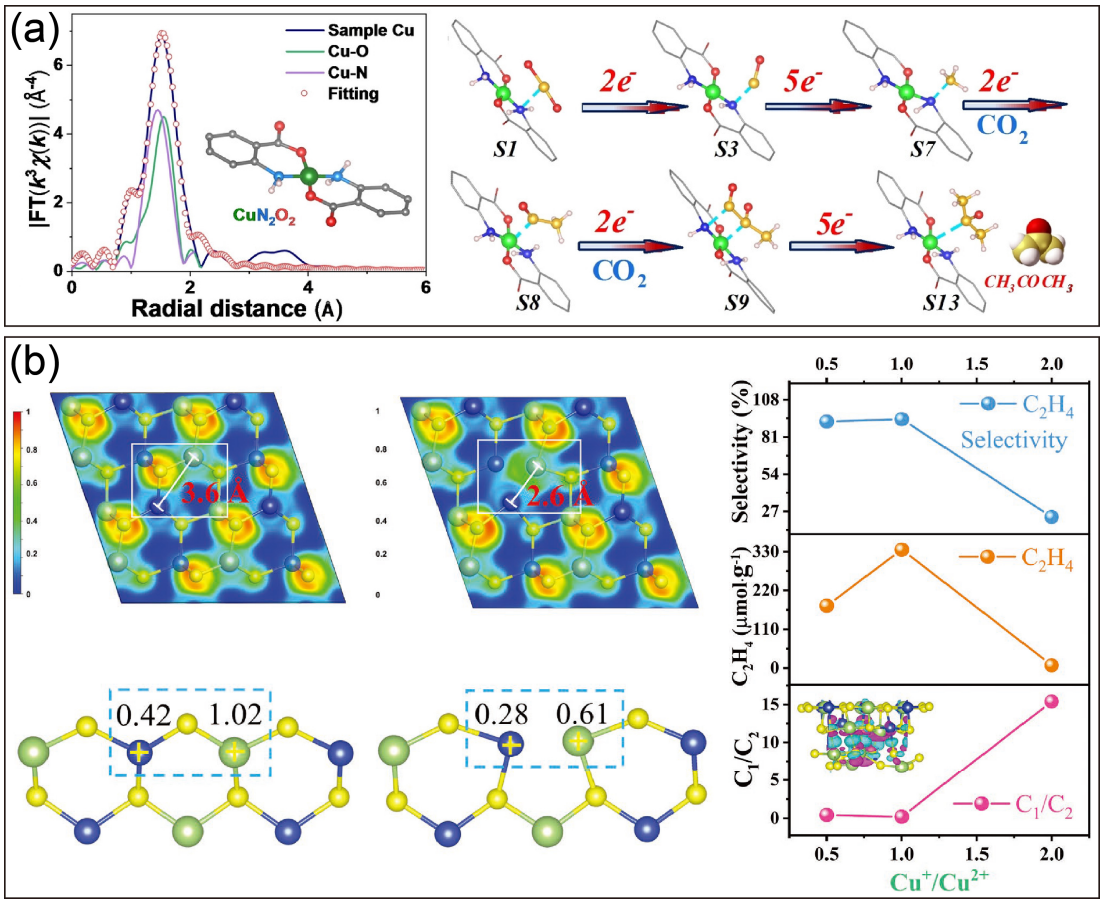

Figure 10. Defect engineering for performance improvement. (**a**) Defective Cu-MOF structure and its mechanism for enhancing acetone production. Reprinted with permission from Ref [119]. Copyright 2024, John Wiley and Sons. (**b**) Sulfur-deficient $CuGaS_2/Ga_2S_3$ and its mechanism for selective ethylene production. Reprinted with permission from Ref. [121]. Copyright 2023, John Wiley and Sons.

4.2. Doping

Doping represents a key strategy for enhancing the performance of photocatalytic CO_2 reduction. By introducing specific elements or defects, the electronic structure of catalysts can be modulated, light absorption efficiency and charge carrier separation can be improved, and consequently, the activity and selectivity of CO_2 reduction can be enhanced. Based on the types of dopants, doping can be categorized into non-metal doping, metal doping, and co-doping.

Several metal-doping strategies have been employed to enhance photocatalytic CO_2 reduction toward C_{2+} products. One effective approach is bimetallic co-doping. For instance, Cu/In co-doping in $AgBiP_2S_6$ (ABPS) modifies the local coordination environment, inducing lattice contraction due to the smaller ionic radii of the dopants (Figure 11a). This structural adjustment elongates the Ag–S bond and exposes more active sites. Consequently, the co-doped catalyst exhibits significantly enhanced activity and selectivity for C_{2+} products, with the exfoliated sample showing a markedly higher C_2H_4 evolution rate than the bulk material (Figure 11b) [124]. Similarly, Cu^+ doping in In_2S_3 induces S vacancies around Cu and In atoms, altering their coordination environments. This enhances charge transfer between Cu–V_S–In sites and adsorbed CO_2 molecules, improves photocatalytic activity, and increases the C_2H_4 yield to 23.4 μmol·h^{-1}·g^{-1} [125]. (2) High-valence doping for constructing solid solutions. For instance, extensive doping of Nb^{5+} into SnO_2 forms $Sn_xNb_{1-x}O_2$ solid solutions. This substitution, accompanied by lattice distortion and V_O generation, results in a shift of the conduction band and synergizes with surface electron-rich states to enhance CO_2 adsorption by 5.7 times. This strategy boosts C_{2+} selectivity to 96.5%, with C_2H_5OH accounting for 87.6%, and increases activity by 19-fold [126]. (3) Single-metal doping primarily encompasses two categories: homometallic heterovalent doping and directional doping. The former strategy aims to construct homometallic heterovalent pair sites, which involves creating adjacent sites consisting of the same metal element with different oxidation states within a single material. For example, in the NiS_2 atomic layer, doping-induced Ni^{n+}-$Ni^{\delta+}$ pair sites result in an asymmetric charge distribution on adjacent

adsorbed *CO intermediates, weakening repulsive interactions and thus achieving 74.3% ethylene selectivity under simulated industrial flue gas conditions [127]. Another representative example is single-metal directed doping. For instance, in-situ doping of low-electronegativity indium atoms reconstructs the local charge distribution of the Cu_2MoS_4 catalyst, enhancing charge enrichment at Mo sites and thereby promoting CO_2 adsorption and dissociation. Studies have shown that the formation of the *COCOH intermediate is a key rate-limiting step in the generation of C_2H_4. Indium doping significantly reduces the reaction energy barrier of this step (from 0.92 eV to 0.74 eV), facilitating ethylene production [100].

Regarding non-metallic doping, in the nitrogen-doped titanium oxynitride (N-Ti-O/V_0) system, nitrogen doping modulates the surface Ti^{2+}/Ti^{3+} ratio to 0.83, optimizing the N-Ti-O/V_0 coordination motif. This synergistic effect generates a strong reductive polarization field, stabilizes Vo by enriching electron-rich intermediates, and enhances charge distribution through the N–Ti–O coordination structure, thereby suppressing the hydrogen evolution reaction and increasing C_2H_2 selectivity to 69.3% [128]. Furthermore, oxygen doping in $FeCoS_2$ atomic layers forms Co–O–Fe triatomic sites. Charge accumulation around the O atoms promotes the adsorption of the HOOC–COOH intermediate and facilitates C–O bond formation. The asymmetric charge distribution at the Co–O–Fe site reduces the C–C coupling energy barrier from 2.10 eV to 1.07 eV, resulting in a C_2H_4 yield of 20.1 $\mu mol \cdot h^{-1} \cdot g^{-1}$ [129].

In summary, doping strategies for enhancing photocatalytic CO_2 reduction to C_{2+} products can be classified into two categories: one involves constructing homometallic sites with different valence states to utilize charge polarization for C–C coupling between adjacent atoms; the other employs heterometallic interfaces to create an asymmetric charge environment, leveraging intrinsic electronic differences between metals to facilitate efficient C–C coupling. Evidence suggests that heterometallic systems often achieve higher activity and selectivity compared to their homometallic counterparts, which is frequently attributed to their stronger inherent charge differences that facilitate *CO intermediate adsorption and coupling [130]. The doping strategy modulates the catalyst's electronic structure through the introduction of foreign elements, creating an asymmetric charge environment that facilitates C–C coupling. This approach is intrinsically connected to other methodologies, as its effectiveness often relies on defect structures to stabilize the incorporated ions. The resulting charge microenvironment further enables the integration of atomic-level active sites or heterojunctions. Practical implementation requires careful consideration of dopant-matrix compatibility to prevent excessive lattice distortion. Consequently, in catalyst design, doping serves as an essential preliminary stage for electronic structure optimization.

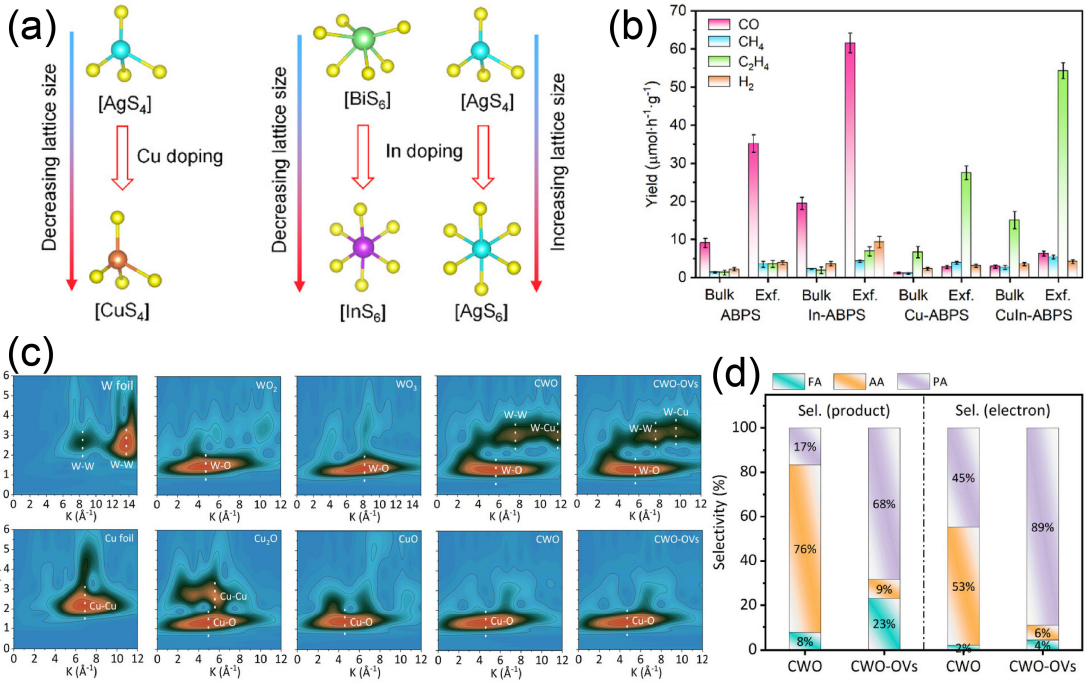

Figure 11. Doping and atomic engineering for performance improvement. (**a**) Cu and In doping mechanism and (**b**) product rates of CuIn-doped $AgBiP_2S_6$. Reprinted with permission from Ref. [124]. Copyright 2025, John Wiley and Sons. (**c**) Cu K-edge and W L-edge EXAFS spectra, and (**d**) product/electron selectivity of $CuWO_4$ with Cu-$Cu^{\delta+}$-$W^{\delta+}$. Reprinted with permission from Ref. [13]. Copyright 2024, John Wiley and Sons.

4.3. Atomic Engineering

To achieve efficient production of C_{2+} products, atomic engineering strategies in the field of photocatalytic CO_2 reduction have gradually expanded from single-atom and diatomic site catalysis to the emerging triple-atom site catalysis, aiming to achieve precise control over the C–C coupling process at the atomic scale. At the single-atom level, researchers have significantly enhanced C_2 product selectivity by constructing novel single-atom tandem photocatalysts and regulating electron interactions through orbital hybridization. For instance, a three-coordinated Cu single atom supported on In_2O_3 increases the electron density near the Fermi level through p–d and d–d orbital hybridization, promoting orbital overlap between the active site and intermediates. This enhances intermediate adsorption, accelerates electron transfer, and effectively weakens repulsive forces during the C–C coupling process [59].

At the diatomic level, asymmetric diatomic sites in Ni–Co/TiO_2 reconstruct the electronic structure near the Fermi level through hybridization of Ni-3d/Co-3d and Ti-3d orbitals. The electronic modulation induced by these dual sites not only enhances light absorption and electron transfer rates but also significantly promotes C–C coupling [13]. Recently, Zhang et al. successfully constructed equidistant double-platinum atom pairs on the surface of Bi_3O_4Br using a metal–porphyrin (Pt–TCPP) molecular aggregation strategy, enabling precise regulation of atomic spacing via van der Waals forces and addressing the issue of random site distribution in conventional synthesis methods. This equidistant diatomic structure effectively promotes C–C coupling, increasing the C_2H_4 yield by 8-fold and the TOF by nearly 10 times. Combined advanced characterization and theoretical calculations revealed the critical role of the diatomic sites in optimizing interfacial charge transfer, reducing the reaction energy barriers of key steps, and stabilizing multi-carbon intermediates, highlighting their kinetic advantages in promoting C_2 product formation [131].

Furthermore, triple-atom site strategies offer greater regulatory potential and synergistic advantages. For instance, an oxygen-vacancy-induced Cu-$Cu^{\delta+}$-W^{6+} triatomic site efficiently promotes C–C coupling for propanoic acid production. Analysis confirms that oxygen vacancies elongate the W–Cu distance and shorten the Cu–Cu bond (Figure 11c), while also generating charge-asymmetric Cu sites. These structural and electronic modifications collectively reduce inter-adsorbate repulsion and enhance reactivity, leading to superior selectivity for liquid products (Figure 11d) [13].

In conclusion, the evolution of catalytic strategies from single-atom to diatomic and triple-atom sites highlights a key trend in the precise design and dynamic regulation of photocatalytic CO_2 reduction systems at the atomic scale. By tailoring atomic structures, electronic properties, and synergistic mechanisms, these approaches not only deepen the understanding of C–C coupling mechanisms but also provide a solid theoretical and experimental foundation for the design of next-generation highly efficient C_{2+} photocatalysts. In catalytic systems, atomic engineering functions as a precise catalytic system or a core active component. Its combination with defect engineering or doping promotes efficient C_{2+} production. For instance, atomic sites often require defects for anchoring, while their tailored electronic properties simultaneously aid charge separation in heterojunctions. Therefore, balancing synthetic precision with structural stability remains a key practical requirement.

4.4. Heterojunction

The construction of heterojunctions is one of the effective strategies for enhancing charge separation and transfer, thereby improving photocatalytic efficiency [132]. In recent years, several innovatively designed heterojunction systems have demonstrated remarkable advantages in photocatalytic CO_2 reduction for C_{2+} production through unique charge separation mechanisms and interfacial engineering. For example, an atypical Type II heterojunction catalyst, Au/TiO_2/MFU-4l, was developed. Through precise anchoring of Au^+/Au nanoparticles at the edge of the TiO_2/MFU-4l interface (via Ti–O–$Au^{+/0}$–O–Zn bonding), the reverse transfer of visible-light-excited holes was achieved, significantly enhancing the hole oxidation capability. This catalyst yielded ethylene at a rate of 107.0 $\mu mol \cdot h^{-1} \cdot g^{-1}$ under simulated sunlight with selectivity exceeding 90%, providing a new mechanism for efficient photocatalytic conversion of CO_2 to C_2H_4 [133]. The Type II R-P25/In_2O_{3-x} heterojunction with oxygen vacancies effectively suppresses carrier recombination and provides a lower reduction potential, facilitating the generation of C_2H_4, C_2H_6, C_3H_6, and C_3H_8, among others. The reaction pathway, confirmed via *in situ* DRIFTS, proceeds through hydrogenation and C–C coupling via the *COOH intermediate [68]. A universal strategy of constructing Z-scheme M_xO_y@Bi_2S_3 heterojunctions (Figure 12a) introduces charge-asymmetric M–Bi pair sites that polarize key intermediates, significantly reducing the C–C coupling barrier and enhancing electron density along the forming C–C bond to selectively promote C_2H_4 formation. Control experiments further confirm that only heterojunctions forming Zn–Bi, In–Bi, and Sn–Bi pairs yield C_2H_4 (Figure 12b), demonstrating the general efficacy of such metal-pair sites in steering CO_2 photoreduction from C_1 to C_2 products [134].

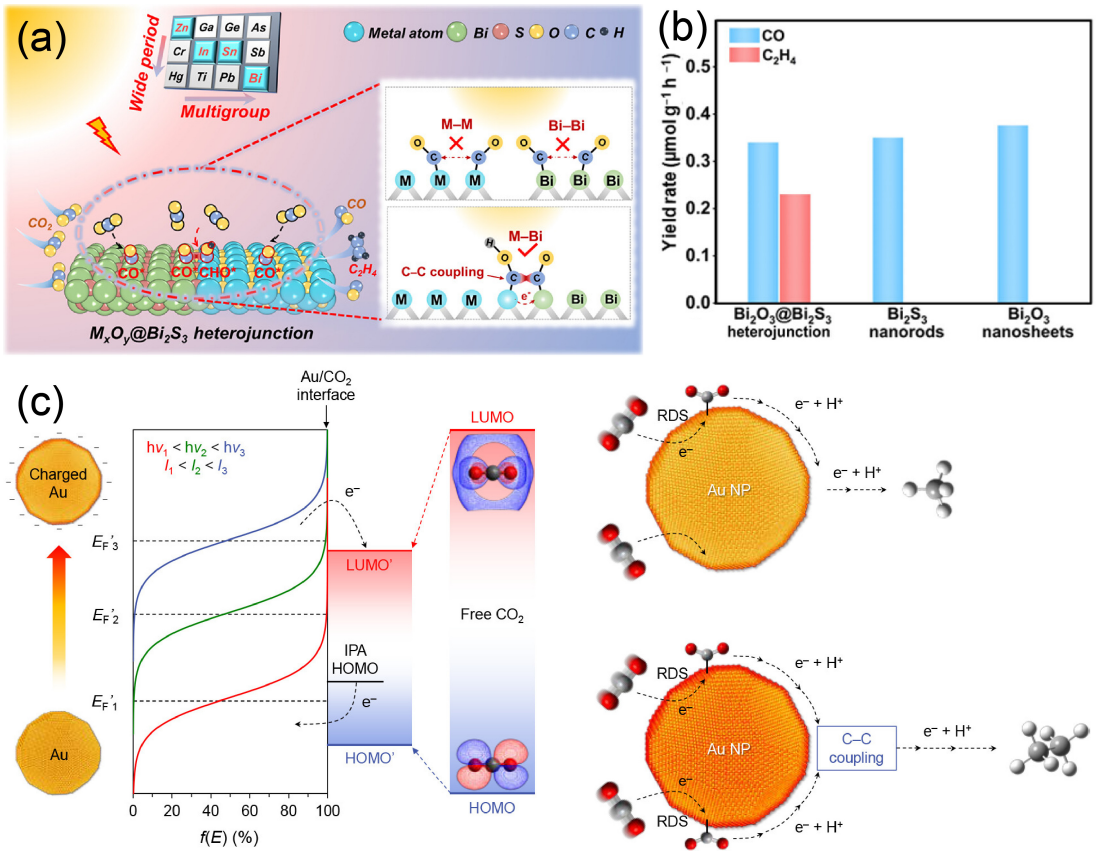

Figure 12. Heterojunction and LSPR for performance improvement. (**a**) Scheme for photocatalytic CO_2 reduction into C_2H_4 with the $M_xO_y@Bi_2S_3$ heterojunction; (**b**) product rates of $M_xO_y@Bi_2S_3$ heterojunction. Reprinted with permission from Ref. [134]. Copyright 2025, American Chemical Society. (**c**) Enhanced photocatalytic CO_2 reduction via LSPR effect of Au nanoparticles. Reprinted with permission from Ref. [135]. Copyright 2018, American Chemical Society.

The synergistic effect between atomic-level regulation and heterojunctions also shows unique advantages. For instance, by integrating Pd single atoms with PdO nanoislands on phosphorus-modified BiOCl, an S-scheme heterojunction (PdO/BiOCl–Pd1) was successfully constructed. The unique S-scheme charge transfer facilitates the formation of electron-rich PdO sites, which serve as efficient C–C coupling sites after adsorbing *CO. The combination of the heterojunction and palladium atomic sites enabled a C_2H_6 yield of 215.6 μmol·h^{-1}·g^{-1}(with 97.5% selectivity) and maintained stability over 200 h [136].

The studies above illustrate that the separation, transport, and utilization of photogenerated carriers can be effectively regulated by carefully designing heterojunction interfaces. Strategies such as constructing atypical Type II or S-scheme charge transfer pathways and introducing charge-asymmetric active sites have been shown to significantly lower the energy barrier and increase the local concentration of critical intermediates for the C–C coupling process. The synergy between interface engineering and atomic-level active centers provides critical insights and a versatile platform for developing efficient and highly selective C_{2+} photocatalytic systems. Heterojunctions provide a platform for combining diverse catalytic strategies. They not only anchor atomic-level active sites but also synergize with doping to enhance charge separation and band structure control. In these complex systems, interfacial quality and structural stability play a decisive role in performance.

4.5. Local Surface Plasmon Resonance

Local Surface Plasmon Resonance (LSPR) refers to the phenomenon in which free electrons on the surface of metal nanoparticles collectively oscillate under resonant light excitation. The LSPR effect can promote carrier separation and facilitate the adsorption and activation of key intermediates through the enhancement of the local electric field and the generation of hot electrons. For instance, Li et al. combined the LSPR effect of Ag with the photoelectric properties of TiO_2, achieving light-driven oxidative coupling of CH_4 and CO_2 under mild conditions to efficiently synthesize C_2H_4 [137]. Devasia et al. confirmed through *in situ* surface-enhanced Raman spectroscopy (SERS) that photoexcitation of the Ag surface can generate C_1–C_4 intermediates, providing experimental support for the feasibility of C–C coupling driven by LSPR [138]. The mechanism underlying LSPR-

driven C–C coupling has been further elucidated. Plasmonic gold nanoparticles facilitate visible-light-driven multi-electron CO_2 reduction in aqueous environments, overcoming the kinetic limitations of C–C coupling for hydrocarbon production. Upon photoexcitation, these nanoparticles act as a source of hot electrons for CO_2 activation. Importantly, the reaction selectivity is governed by a Poisson statistical model of electron harvesting: high photon energy and flux enable simultaneous multi-electron transfer, which promotes C–C coupling and the formation of C_{2+} hydrocarbons such as ethane (Figure 12c) [135].

Lattice defects can induce the generation of free carriers, which in turn trigger localized photothermal and electronic effects, collectively optimizing the reaction microenvironment. For example, Lu et al. synthesized tungsten oxide (WO_{3-x}) via an acid-assisted solvothermal method, resulting in an amorphous surface structure rich in oxygen vacancies and low-valent tungsten ions. HAADF-STEM observations confirmed the abundant defect states. Photocatalytic results indicated that these defect-mediated photothermal effects and photoelectron injection act synergistically to promote the reduction of CO_2 to ethylene [139]. Notably, in response to the issue of O_V in non-metallic plasmonic photocatalysts being prone to oxidation and exhibiting poor stability, recent studies have proposed a "photoelectron injection" strategy. By constructing a $W_{18}O_{49}$/ZIS composite photocatalyst, the O_V sites in $W_{18}O_{49}$ are effectively protected via interfacial photoelectron injection, and a local multi-electron environment is created to extend the hot-electron lifetime. Theoretical calculations indicate that this strategy significantly enhances CO_2 adsorption, reduces the energy barriers for the formation of the key intermediate *COH (0.054 eV) and for CO–COH coupling (0.574 eV), and promotes the reaction pathway toward C_2H_6 formation [79]. Yang et al. attribute the enhanced photocatalytic conversion of CO_2 to C_2H_6 to the LSPR effect. In their system, LSPR-generated hot electrons lower the sulfur vacancy formation energy in ZIS to create active sites and inject into the semiconductor, prolonging the carrier lifetime from 2.78 ps to 6.89 ps to inhibit recombination. Consequently, the Z-M20 catalyst achieves 92.0% C_2H_6 selectivity by sustaining the multi-electron C–C coupling process [140]. The photoexcitation parameters of LSPR provide a new avenue for regulating reaction pathways. Studies show that multi-electron transfer in plasmonic metals such as Au NPs can be directed by tuning the photon energy and light intensity. For instance, in CO_2 reduction, achieving C–C coupling to form C_2H_6 necessitates both a short wavelength (≤488 nm) and a threshold light intensity (≥300 $mW \cdot cm^{-2}$). Any deviation from these conditions (e.g., longer wavelength or lower intensity) inhibits this pathway, highlighting the critical influence of optical parameters on reaction selectivity [135].

A summary of the literature on LSPR indicates that established insights into C_1 product formation offer valuable guidance for C_2 synthesis. Tuning the size, morphology, and composition of plasmonic metal nanostructures allows optimization of the LSPR effect, thereby controlling the yield and energy distribution of hot electrons to supply essential energy and electrons for C–C coupling. Defect engineering and heterostructure construction facilitate the modification of semiconductor carriers, optimization of band structures and surface states, promotion of hot electron injection, and strengthening of intermediate adsorption, collectively enhancing CO_2 reduction performance. Furthermore, core–shell architectures improve interfacial coupling and stability between plasmonic metals and semiconductors while inhibiting photocorrosion. The resulting Schottky barrier suppresses carrier recombination, extends hot electron lifetimes, and establishes a favorable microenvironment for multi-electron reactions such as C–C coupling and multi-step reduction. However, the effective utilization of LSPR generally depends on integration with other components. In catalyst design, LSPR therefore functions as a tunable energy-input element that works synergistically with heterojunctions and defect engineering to construct optimized microenvironments for multi-electron reactions.

4.6. Dual-Function System Optimization

4.6.1. Photothermal Catalysis

Photothermal catalysis utilizes photon energy and converts unabsorbed light into thermal energy, which accelerates reaction kinetics at lower overall temperatures and enhances reaction selectivity by regulating key steps such as CO_2 adsorption, intermediate formation, and C–C coupling [45]. This process requires balancing light intensity and temperature to optimize performance [141]. Current research on the photothermal catalytic synthesis of C_{2+} products primarily focuses on compounds including C_2H_4, C_2H_6, CH_3CH_2OH, C_3H_8, C_3H_6, C_4H_8, and C_4H_{10}. Photothermal co-catalysis is the predominant approach. The main process involves the reverse water-gas shift (RWGS) reaction to hydrogenate CO_2 and reduce it to *CO, followed by further conversion of *CO and H_2 into C_{2+} products via the Fischer–Tropsch synthesis (FTS) pathway. A key challenge lies in overcoming the limitations of traditional single-mode catalysis—particularly the high recombination rate and slow reaction kinetics of photogenerated charge carriers—through rational design of photothermal materials and integrated catalytic strategies [142].

In recent years, numerous studies have demonstrated effective material designs and mechanistic innovations. For example, the in-SV-Bi active site in the Bi_2S_3@In_2S_3 catalyst synergizes with photothermal energy to achieve efficient conversion of CO_2 to C_2H_4 [143]. The Cu/Cu_2Se–Cu_2O heterojunction nanosheet array (Cu-CSCO HNA) constructed by Li et al. enables photothermal catalysis of CO_2 to ethanol under visible to near-infrared light without external heating [144]. Constructing heterojunctions with complementary functions presents an effective strategy for complex tandem reactions. For instance, Peng et al. anchored single-atom Pt on a zirconium-tungsten oxide heterostructure (Pt/(Zr-W)Ox) for the photocatalytic conversion of CO_2 into C_2H_4. In this system, *CO generated at the Pt/ZrO_2 interface migrates to the Pt/WOx region to undergo C–C coupling. Simultaneously, the electron-deficient W site at the Zr–O–W interface acts as a Lewis acid to promote H_2O dissociation, supplying active hydrogen atoms that significantly lower the energy barriers for key intermediates (Figure 13a). This cooperative mechanism achieved a high C_2H_4 yield of 242 μmol·g^{-1} with 83.9% electron selectivity under focused sunlight, showcasing an efficient hydrogen-supplying tandem system [145].

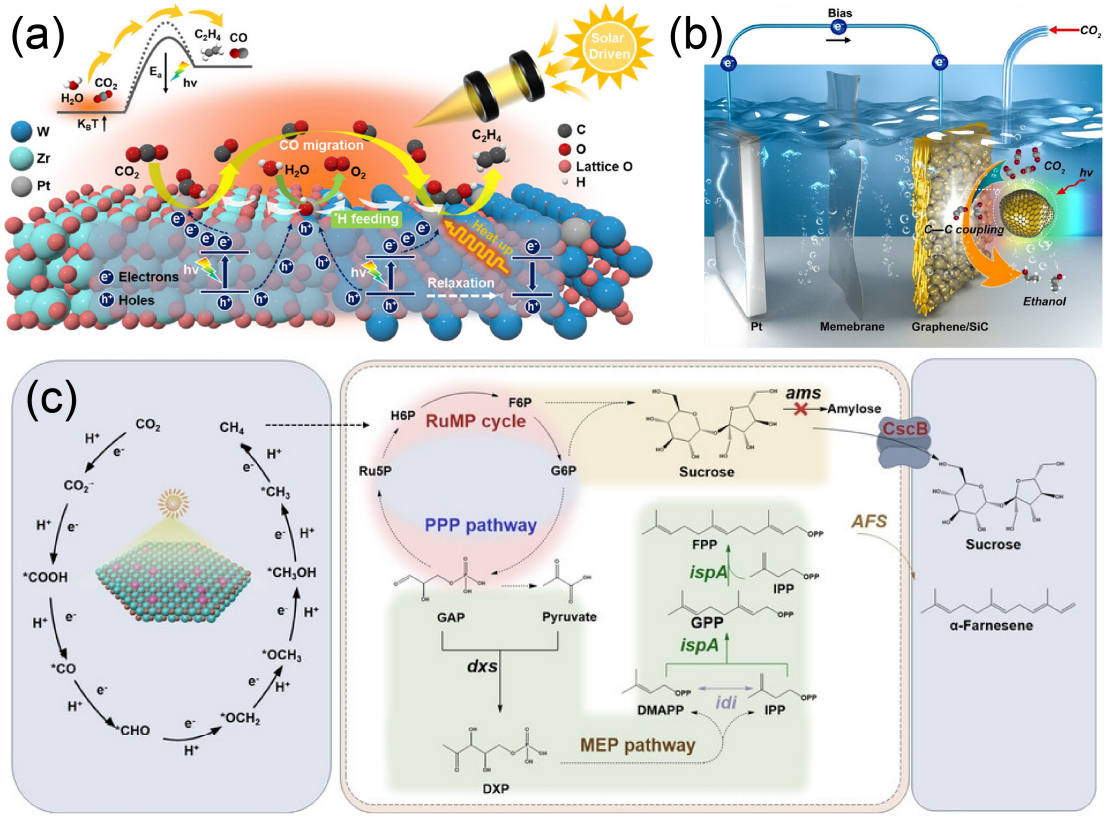

Figure 13. Dual-Function System Optimization. Schematic illustrations for CO_2 reduction with (**a**) photothermal catalysis. Reprinted with permission from Ref. [145]. Copyright 2025, American Chemical Society. (**b**) Photoelectrocatalysis. Reprinted with permission from Ref. [146]. Copyright 2023, John Wiley and Sons. (**c**) Photobiocatalysis. Reprinted with permission from Ref. [147]. Copyright 2025, John Wiley and Sons.

On the other hand, the synergy between photothermal effects and heterojunctions also offers new pathways for performance enhancement. For instance, in a Cu_2O@CuS@SnS_2 core–shell structure, the photothermal effect of the CuS layer triggers a phase transition of SnS_2 from 2H to 1T. Simultaneously, close interfacial contact among SnS_2, CuS, and Cu_2O establishes efficient electron channels, enabling abundant photogenerated electrons from the Cu_2O framework to supply the photothermal catalytic system. More importantly, band bending induced by the built-in electric field leads to the formation of an S-scheme heterojunction between CuS and SnS_2. This structure prolongs carrier lifetime and enhances C_2H_6 yield [76]. Song et al. proposed a novel strategy of photochemicity-triggered synergistic photothermal enhancement for CH_4 oxidative coupling. In the Au/x%CeO_2/ZnO catalyst, Au and CeO_2 collectively capture photogenerated electrons from ZnO to promote O_2 activation, significantly reducing the dissociation energy barrier of the first C–H bond in CH_4 through synergy. This accelerates the rate-determining step. Additionally, the photothermal effect of Au NPs effectively promotes desorption of ·CH_3 radicals and inhibits over-oxidation, thereby facilitating C_2H_6 generation [148]. Photothermal catalysis transcends mere thermal enhancement by selectively lowering energy barriers in critical steps such as C–H activation and *CO coupling through targeted photon-to-thermal conversion. The product selectivity in these processes, ranging from C1 to C_{2+}

compounds, is highly dependent on the catalyst's ability to control intermediate binding energies and reaction pathways [149–152].

4.6.2. Photoelectrocatalysis

Current research on the photoelectrocatalytic conversion of CO_2 to C_{2+} products primarily focuses on Cu-based photocathode materials, including Cu [153], CuO, and Cu_2O [154]. However, these materials suffer from high energy barriers for C–C coupling and proton-coupled electron transfer (PCET), which forces the reaction to proceed at high overpotentials with low selectivity toward C_{2+} products.

Besides Cu-based materials, certain non-Cu-based catalysts, such as TiO_2, ZnO, and WO_3, have also achieved high C_{2+} product selectivity through structural modulation, though they typically require operation at more negative potentials. Known reaction pathways ultimately yield products spanning C_1 species (CO, $HCOO^-$, HCHO, CH_3OH, CH_4), C_2 compounds (CH_3COOH, CH_2OHCHO, CH_2OHCH_2OH, CH_3CHO, C_2H_4, CH_3CH_2OH), and C_3 products (n-$CH_3CH_2CH_2OH$, CH_3COCH_3). Among these, the yield of C_{2+} products such as C_2H_4, C_2H_6, C_3H_6, and C_3H_8 can reach millimolar levels, with Faradaic efficiencies ranging from 20% to 99% [146]. Researchers are now adopting multiple synergistic strategies to enhance the performance of photoelectrocatalytic CO_2 reduction toward C_{2+} products. Several key strategies have been developed to enhance the performance of photoelectrocatalytic CO_2 reduction toward C_{2+} products, including heteroatom doping as exemplified by Ga-Cu_2O [155] and Ce-TiO_2 [156]; cocatalyst modification such as Ag/Pd [150] and M/BiOCl (M = Au, Pd, Pt) [157]; interface engineering through either heterogeneous interfaces (e.g., Ag/Cu^+/Cu^0 [158]) or heterojunction construction such as GDY/In_2O_3 [159]; along with confined cooperative catalytic structures such as MOF–COF hybrids [115].

The rational design of material interfaces itself serves as a powerful approach to boosting C_{2+} selectivity. A prominent example is reported by Feng et al., whose graphene/silicon carbide composite features an interfacial layer that efficiently directs photogenerated electrons from the SiC substrate to active sites on graphene, thereby enhancing CO_2 activation and C–C coupling for highly selective ethanol production (>99% selectivity, 17.1 $mmol \cdot gcat^{-1} \cdot h^{-1}$ conversion rate) (Figure 13b) [144]. Beyond material design, systematic reaction engineering and condition optimization are equally critical for enhancing C_{2+} selectivity. For example, Andreio et al. employed glycerol oxidation (GOR) instead of the oxygen evolution reaction (OER) to overcome anode reaction energy barriers. By coupling high-photovoltage perovskite with highly selective copper nanoflower (CuNF) catalysts, they achieved bias-free CO_2 reduction for the first time and innovatively proposed a "current density matching" principle. Their work reveals how tuning the catalyst geometric area regulates selectivity, enabling high C_{2+} product selectivity even at high current densities [97]. Furthermore, extending the reaction path or residence time can promote C_{2+} formation, with product distribution being co-regulated by electrolyte composition, catalyst active sites, and applied bias. Advancements in catalyst design, including the engineering of single-atom sites, bimetallic clusters, and local microenvironments, coupled with data-driven synthesis strategies, are pivotal to enhancing activity and selectivity [160–165].

4.6.3. Photobiocatalysis

Photobiocatalysis achieves the conversion of CO_2 into products such as acetic acid and acetoin by coupling photocatalysis with biosynthetic systems. This strategy utilizes light energy to drive the initial reduction reaction and takes advantage of the high selectivity of microorganisms or enzymes to complete the construction of complex carbon chains, providing a new approach for the sustainable conversion of carbon resources.

Two representative strategies have emerged in this field. The first is the tandem system combining photocatalysis and biosynthesis. For instance, Yu et al. reported a transition metal-doped ZnO (M–ZnO) photocatalyst that efficiently reduces CO_2 to CH_4. Subsequently, CH_4 was converted into sucrose or α-farnesene with the aid of genetically engineered methane-oxidizing bacteria, offering a novel pathway for the green synthesis of long-chain carbon compounds (Figure 13c) [147]. The second strategy involves hybrid systems integrating microorganisms and photocatalysts. Su et al. innovatively proposed an abiotic–biological domino cascade strategy by coupling a photocatalytic syngas production system from CO_2 with adaptively evolved syngas-fermenting strains, enabling efficient conversion of CO_2 to C_2 products such as acetic acid and ethanol. Directed modification of *Clostridium ljungdahlii* via adaptive laboratory evolution (ALE) resulted in an evolved strain, which exhibited a 2.5-fold increase in growth rate and a 120-fold enhancement in C_2 product yield under continuous-flow conditions [166]. For example, researchers employed a photocatalyst sheet composed of La- and Rh-co-doped $SrTiO_3$ and Mo-doped $BiVO_4$ to photolyze water under mild conditions to produce H_2, which supplied electrons and hydrogen sources for the carbon-fixing bacterium *Sporomusa ovata*, thereby selectively converting CO_2 into acetic acid [167].

In addition, coordinated regulation of electron transport and metabolic pathways has become a research focus. Some researchers have developed an eosin Y–*Ralstonia eutropha* biohybrid system. Through spontaneous anchoring of the photosensitizer eosin Y on membrane-bound hydrogenase, directed transfer of photogenerated electrons is achieved to generate H_2 intermediates, which are further reduced by hydrogenase to form NADH and drive CO_2 reduction. Combined with metabolic engineering modifications, non-oxygen-dependent proton pumps (e.g., *Gloeobacter* rhodopsin) were introduced to enhance ATP synthesis, while biosynthetic pathways for L-lactic acid and acetic acid were blocked to redirect carbon flux toward acetoin production [168]. Chen et al. reported a solar-decoupled biohybrid strategy that uses continuous photocatalysis to store solar energy during the day and release it in the form of electrons at night, providing an uninterrupted energy supply for photosynthetic microorganisms. This approach enables all-weather CO_2 fixation and long-chain compound biosynthesis, offering a new perspective for sustainable biomanufacturing and potential avenues for high-value long-chain compound synthesis by photosynthetic microorganisms [169]. The dual-function system, which integrates photothermal, photoelectric, and photobiocatalytic processes, broadens the functional scope of photocatalysis by incorporating additional physical fields or reaction pathways. These systems work in concert with the strategies mentioned above. While defects, doping, and atomic-level designs modulate active sites at the micro level, dual-function systems regulate energy and reaction pathways from a macro perspective.

5. Conclusions and Prospects

5.1. Conclusions

(1) Current research on the photocatalytic reduction of CO_2 to C_{2+} products focuses on optimizing catalyst active sites and reaction conditions through multiple synergistic strategies to achieve efficient and highly selective conversion. The key research emphasis lies in regulating the adsorption state and hydrogenation pathway of C_1 intermediates to facilitate C_1–C_1 coupling or the stepwise transformation of C_1–C_2 species. By means of in-situ infrared spectroscopy, Raman spectroscopy, X-ray absorption spectroscopy, and time-resolved surface-enhanced infrared techniques, the evolution of key intermediates can be tracked in real time, while the mechanisms of active centers—such as charge-polarized dual sites and single atoms—are elucidated with the aid of DFT calculations. Although significant progress has been made in the selectivity of higher-carbon products, those currently achieving high selectivity are still mainly limited to C_2 species (e.g., C_2H_6, C_2H_4, C_2H_5OH, CH_3COOH). Reports on C_3 and higher products (such as propanol, propylene, and butanol) remain relatively scarce. This is primarily because the generation of C_3 products not only requires stabilization of C_1 intermediates but also the construction of suitable active sites that can facilitate efficient coupling between C_1 and C_2 intermediates.

(2) Current strategies for enhancing CO_2 reduction to C_{2+} products mainly include three aspects: First, constructing charge-asymmetric active sites to improve the thermodynamic environment for C–C coupling by weakening the electrostatic repulsion between adjacent *CO intermediates. Essentially, this approach relies on precise orbital interactions between sites, where the adsorption and activation behaviors of intermediates can be optimized through orbital-matched structural design. Second, promoting the separation and transfer of photogenerated charges to enhance the selectivity for C_{2+} products. This strategy requires maintaining a high concentration of photogenerated electrons and readily accessible protons at the reaction interface to drive the multi-electron–proton reduction process. Third, stabilizing key intermediates and reducing their formation and transformation energy barriers to facilitate efficient C–C coupling, thereby enhancing both the selectivity and yield of C_{2+} products.

(3) In terms of reaction mechanism studies, a variety of in-situ characterization and theoretical calculation methods are employed to reveal the evolution pathways of key intermediates and the nature of active sites. In-situ diffuse reflectance infrared Fourier transform spectroscopy (DRIFTS) can track the adsorption configuration and dynamic evolution of intermediates during the reaction, providing experimental evidence for the protonation of C_1 species and C–C coupling. However, its detection of gaseous or weakly adsorbed species remains limited. In-situ Raman spectroscopy can identify surface chemical bond vibrations and intermediate species, helping to clarify the formation and transformation pathways of charge-polarized active sites. Nevertheless, it exhibits low sensitivity to low-frequency modes related to C–C coupling and is susceptible to interference from solvent backgrounds. In-situ X-ray photoelectron spectroscopy (XPS) can precisely track changes in the chemical states of surface elements, offering support for the role of charge polarization in promoting C–C coupling. However, its detection depth is relatively shallow (approximately 2–10 nm), making it difficult to obtain sufficient bulk-phase structural information. In practice, quasi-in-situ modes are often adopted to minimize interference from light. DFT calculations can simulate the adsorption

energy, reaction energy barriers, and charge transfer behavior of intermediates, providing a theoretical basis for C–C coupling pathways. However, most existing calculations are based on ideal surface models and often do not fully account for solvation effects. Additionally, the computational cost is relatively high when dealing with complex reaction networks. In-situ X-ray absorption spectroscopy (XAS) can resolve the evolution of the local coordination structure and electronic structure regulation mechanisms of active centers, though its spatial resolution is limited, making it challenging to directly correlate with the dynamic evolution of specific intermediates.

5.2. Outlook

The photocatalytic conversion of carbon dioxide into high-value C_{2+} products is widely regarded as a critical step toward achieving artificial photosynthesis. However, a major challenge hindering the practical application of this technology is the severe imbalance between the overall cost of the catalytic system and the final product yield, which significantly restricts its large-scale development. To overcome this bottleneck, coordinated efforts are required across multiple areas, including material design, mechanistic studies, and system optimization.

At the material level, the primary goal is to design low-cost and highly selective catalysts. Research should shift away from simply replacing precious metals and instead focus on the precise construction of an active central microenvironment. For reaction systems, it is essential to build a catalytic environment with low background interference and high mass transfer efficiency to meet both environmental and economic requirements. In mechanistic studies, clarifying the dynamic process of C–C coupling can provide fundamental insights for the rational design of catalysts and the optimization of reaction systems. Furthermore, establishing standardized performance evaluation protocols, advancing reactor engineering and integration, and incorporating emerging tools such as artificial intelligence are all crucial to supporting the continued development of this technology. The following sections will discuss these aspects in detail.

5.2.1. Product Verification

In photocatalytic CO_2 reduction research, existing studies have shown that even when using $^{13}CO_2$ as the carbon source, ^{12}C-containing products can still be detected. This suggests potential carbon contamination from catalyst precursors, organic solvents, or impurities within the reaction system. Such background carbon signals cannot be ignored. Therefore, the sole detection of carbonaceous products, in the absence of rigorous control experiments, cannot serve as definitive evidence of CO_2 reduction. To ensure data reliability, it is essential to establish a standardized verification system for carbon sources and products. This includes using ^{13}C isotope labeling coupled with online mass spectrometry to accurately track carbon pathways; monitoring reaction pathways in real time via *in situ* infrared and Raman spectroscopy; developing carbon-free synthesis strategies or supercritical CO_2 purification processes to eliminate carbon contamination at the source; and integrating multi-dimensional characterization techniques for systematic product validation. Additionally, simultaneous detection of oxidation products, stoichiometric verification based on carbon balance, and accurate determination of quantum efficiency and production rates are recommended to minimize the impact of reaction condition variations on performance evaluation.

5.2.2. Catalyst Design

Research on converting CO_2 to C_{2+} products is progressing from single-method optimization toward the integration of multiple complementary functions. Current studies focus on three main aspects. In electronic structure regulation, defect engineering, doping, and atomic-level structural design are used to construct charge-asymmetric active sites. These sites optimize intermediate adsorption through precise orbital interactions, effectively reducing electrostatic repulsion between adjacent *CO species and improving the reaction conditions for C–C coupling. In charge behavior regulation, heterojunctions or plasmonic effects enable directional separation and transfer of photogenerated charges, continuously supplying electron and proton flows for multi-step proton–electron transfer processes. In reaction microenvironment design, hierarchical pore structures and photothermal–photoelectric dual-function systems help regulate the local concentration and residence time of intermediates, thereby stabilizing key active species and lowering their transformation energy barriers.

Significant synergy exists among these functional aspects. The design of future high-performance catalysts should focus on integration across levels rather than simple method combination. For example, combining heterojunctions, which enable macroscopic charge transport, with atomic-level designs that precisely position coupling sites, can establish an efficient “charge supply–surface coupling” mechanism. This systematically resolves the matching issue between electron supply and surface reaction kinetics. Interactions between different

strategies require careful evaluation. Although combining plasmonic materials with heterojunctions provides both hot electron injection and built-in electric field-driven charge separation, improper regulation of the interfacial Schottky barrier can hinder hot electron transfer and degrade overall performance. Therefore, successful catalyst design depends not only on selecting suitable methods but also on understanding their interactions and precisely controlling interfacial properties such as the Schottky barrier.

5.2.3. Research on Reaction Mechanisms and Characterization Techniques

Significant challenges remain in understanding the reaction mechanisms of photocatalytic CO_2 reduction to C_{2+} products. Current experimental techniques face limitations in both temporal and spatial resolution. They cannot adequately track transient intermediates at nanosecond to femtosecond timescales, nor directly observe atomic-scale structural changes under realistic reaction conditions. Simultaneous monitoring of electron transfer and surface reactions during photocatalytic operation presents additional difficulties. Theoretical approaches also show important limitations. Most simulations focus on ground-state thermodynamics while providing insufficient treatment of excited-state dynamics. Existing multiscale simulation methods need further refinement, particularly for understanding the dynamic energy barriers involved in photogenerated carrier-mediated C–C coupling.

Addressing these challenges requires progress in three interconnected areas. First, we need to develop characterization methods with high spatiotemporal resolution under working conditions. This could involve combining femtosecond X-ray absorption spectroscopy with transient surface-enhanced Raman spectroscopy, or integrating environmental transmission electron microscopy with four-dimensional electron microscopy in illuminated reactive environments. Advances in synchrotron soft X-ray spectroscopy and single-molecule fluorescence imaging would enable real-time observation of active site dynamics and intermediate transformations. Second, theoretical methods should advance to simulate photoexcited-state dynamics. This requires multiscale models that combine time-dependent density functional theory with non-adiabatic molecular dynamics. We need computational protocols specifically designed for light-driven C–C coupling processes and dynamic energy barrier calculations. Developing hybrid quantum mechanics/molecular mechanics frameworks that incorporate microscopic reaction dynamics would be valuable. Machine learning potentials derived from first-principles calculations could significantly improve computational efficiency for simulating photogenerated carrier behavior and surface reactions. Third, deeper integration of experimental and theoretical approaches through data-driven methodologies is essential. Implementing deep learning algorithms could help establish relationships between spectral features, structure, and catalytic activity. Advanced time-series analysis and predictive multiscale mechanism models would strengthen the connection between theory and experiment. Establishing open catalytic databases would accelerate the validation cycle for new mechanistic insights.

5.2.4. Development of Dual-Functional Synergistic Strategies

The production of multi-carbon compounds via photothermal, photoelectrochemical, and photobiological CO_2 reduction still faces significant challenges in activity, selectivity, and stability. Photothermal catalytic systems currently exhibit relatively low CO_2 conversion rates, predominantly yielding C_1 products, with limited selectivity toward C_{2+} compounds. They also suffer from sintering and carbon deposition under high-temperature conditions, leading to poor stability. Photoelectrocatalysis improves charge separation and transport through interface engineering, yet remains constrained by complex material fabrication, high costs, the need for external bias, and insufficient photoelectrode stability. Understanding of the C–C coupling mechanism in these systems is still inadequate, highlighting the need for developing efficient, stable, and low-cost electrocatalysts and light-absorbing components. Photobiocatalysis offers advantages such as mild reaction conditions and product diversity, but is limited by low efficiency, slow extracellular electron transfer, poor microbial tolerance, and difficult product separation, all of which hinder large-scale application.

For photothermal and photoelectrocatalytic systems, future work should focus on designing catalysts that optimize intermediate adsorption and activation and promote C–C bond formation through precise control of the active-site microenvironment. Concurrently, strategies to mitigate structural degradation, active component aggregation, or leaching are essential to enhance stability. Scalable and controllable synthesis methods for high-performance catalysts must also be developed. For photobiological systems, metabolic engineering and synthetic biology approaches should be employed to redesign carbon flux pathways, enhance electron transfer, and improve microbial robustness.

5.2.5. Reactor Design and System Integration

Current research on photocatalytic CO_2 reduction remains largely confined to laboratory scale. Inadequate mass transfer efficiency and uneven light distribution in reactor designs are key limiting factors, particularly in high-concentration catalyst slurries or fixed-bed systems, where mass transfer resistance between CO_2 and protons significantly affects reaction kinetics and product selectivity.

To address these issues, novel reactor designs such as microchannel reactors, photoelectrochemical coupling systems, and computational fluid dynamics-optimized architectures should be developed. Recent innovations, including wireless photocatalyst sheets, pilot-scale solar thermal reaction systems, membrane reactors, concentrator reactors, and flow reactors inspired by electrocatalysis, have demonstrated potential for enhancing C_{2+} selectivity by improving light distribution and reactant transport. The feasibility of large-scale operation has been preliminarily validated in a 100 m^2 photocatalytic water-splitting demonstration system.

However, large-scale photocatalytic systems still suffer from low energy conversion efficiency and insufficient catalyst stability. Future efforts should focus on enhancing light capture and utilization, for example, via optical focusing technologies to intensify local light intensity, and holistically improving system energy efficiency to facilitate the practical application of photocatalytic CO_2 reduction.

5.2.6. Artificial Intelligence and Machine Learning

The application of artificial intelligence and machine learning in photocatalytic CO_2 reduction remains at an early stage. Current research primarily focuses on C_1 products, but the methodologies and approaches developed show significant promise for advancing the study of C_{2+} products. Existing work mainly addresses three areas: catalyst design, reaction mechanism exploration, and efficient screening. In catalyst design, machine learning improves screening efficiency through structure-activity relationship models [170]. By analyzing key descriptors such as metal electronegativity, coordination environment, and d-band center position, these models can predict the adsorption behavior and dimerization trends of *CO intermediates. This provides theoretical guidance for designing catalysts with superior C–C coupling performance [171]. For reaction mechanism studies, machine learning methods enable direct prediction of multi-carbon coupling pathways. Research demonstrates that models trained on C_1 and C_2 reaction data can effectively predict energy barriers for C_3 pathways, aiding understanding of long carbon chain formation mechanisms [172].

In efficient screening, simplified feature models have enhanced prediction efficiency. The WLEDZ model, which incorporates only five key features (work function, local electronegativity, interplanar spacing, and atomic number), maintains good accuracy in predicting intermediate adsorption energies. This provides a feasible approach for rapid screening of bimetallic catalysts [173]. Future work should prioritize developing specialized experimental databases for photocatalytic CO_2 reduction, creating learning algorithms suitable for limited data scenarios, and establishing cross-scale computational platforms. These initiatives will advance CO_2-to-C_{2+} conversion research from empirical exploration toward rational design.

Funding

We would like to acknowledge the support from the National Natural Science Foundation of China (22406085), the Natural Science Foundation of Jiangsu Province (BK20241239), the Youth Talent Support Program of Jiangsu Association for Science and Technology (JSTJ-2024–056), and the National Natural Science Foundation of China (225B1013).

Conflicts of Interest

The authors declare no conflict of interest.

References

1. Dang, H.; Guan, B.; Zhu, L.; et al. A Review on Photocatalytic and Electrocatalytic Reduction of CO_2 into C_{2+} Products: Recent Advances and Future Perspectives. *Energy Fuels* **2025**, *39*, 10109–10133.
2. Wang, Y.; Chen, E.; Tang, J. Insight on Reaction Pathways of Photocatalytic CO_2 Conversion. *ACS Catal.* **2022**, *12*, 7300–7316.
3. Zhang, Y.; Liu, Y.; Li, H.; et al. Regulating local charge distribution of single Ni sites in covalent organic frameworks for enhanced photocatalytic CO_2 reduction. *Chem. Eng. J.* **2024**, *489*, 151479.
4. Lin, C.-C.; Huang, S.-K.; Tseng, W.-N.; et al. Chirality-Regulated Spin-Polarization of Perovskite Nanoplates for Photocatalytic CO_2 Reduction Reaction. *J. Am. Chem. Soc.* **2025**, *147*, 40347–40355.

5. Luo, H.; Lu, X.; Cao, Y.; et al. Boosted CO_2 Photoreduction Performance by CdSe Nanoplatelets via Se Vacancy Engineering. *Adv. Sci.* **2025**, *12*, 2413684.
6. Hong, L.; Zhang, H.; Hu, L.; et al. Near-infrared light–driven biomass conversion. *Sci. Adv*. **2024**, *10,* eadn9441.
7. Xu, F.; Zhao, F.; Deng, X.; et al. Integrating S-scheme photocatalysis with tandem carbonylation: A green and scalable strategy for CO_2 valorization. *Nat. Commun.* **2025**, *16*, 6882.
8. Jin, P.; Guo, P.; Luo, N.; et al. Photochemical H_2 dissociation for nearly quantitative CO_2 reduction to ethylene. *Science* **2025**, *389*, 1037–1042.
9. Wang, H.; Song, L.; Lv, X.; et al. Low-Coordination Triangular Cu_3 Motif Steers CO_2 Photoreduction to Ethanol. *Angew. Chem. Int. Ed*. **2025**, *64*, e202500928.
10. Chen, C.; Ye, C.; Zhao, X.; et al. Supported Au single atoms and nanoparticles on MoS_2 for highly selective CO_2-to-CH_3COOH photoreduction. *Nat. Commun*. **2024**, *15*, 7825.
11. Gong, S.; Niu, Y.; Liu, X.; et al. Selective CO_2 Photoreduction to Acetate at Asymmetric Ternary Bridging Sites. *ACS Nano* **2023**, *17*, 4922–4932.
12. Shen, Y.; Ren, C.; Zheng, L.; et al. Room-temperature photosynthesis of propane from CO_2 with Cu single atoms on vacancy-rich TiO_2. *Nat. Commun*. **2023**, *14*, 1117.
13. Su, H.; Yin, H.; Orbell, W.; et al. Asymmetric Triple-Atom Sites Combined with Oxygen Vacancy for Selective Photocatalytic Conversion of CO_2 to Propionic Acid. *Angew. Chem. Int. Ed*. **2025**, *64*, e202425446.
14. Huang, F.; Wang, F.; Liu, Y.; et al. Cu-ZnS Modulated Multi-Carbon Coupling Enables High Selectivity Photoreduction CO_2 to CH_3CH_2COOH. *Adv. Mater*. **2025**, *37*, 2416708.
15. Li, W.; Liu, Z.; Rhimi, B.; et al. Nitrogen-Bridged S–N–Cu Sites for CO_2 Photoreduction to Ethanol with 99.5% Selectivity in Pure Water. *Angew. Chem. Int. Ed*. **2025**, *64*, e202423859.
16. Huang, X.; Chen, Y.; Xie, X.; et al. Covalent Organic Frameworks with Tunable Bridge Positions for Photocatalytic CO_2 Reduction to Propylene Under Visible Light Illumination. *Small* **2025**, *21*, 2408817.
17. Wang, L.; Liu, Y.; Perumal, S.; et al. Enhancing photocatalytic CO_2 reduction to butanol by facet-dependent interfacial engineering of CeO_2/Cu_2O. *Appl. Catal. B Environ*. **2025**, *368*, 125122.
18. Li, C.; Wang, J.; Tong, L.; et al. Recent progress and challenges of photocatalytic CO_2 conversion into value-added multi-carbon products. *Coord. Chem. Rev.* **2024**, *502*, 215623.
19. Lyu, W.; Liu, Y.; Zhou, J.; et al. Modulating the Reaction Configuration by Breaking the Structural Symmetry of Active Sites for Efficient Photocatalytic Reduction of Low-concentration CO_2. *Angew. Chem. Int. Ed*. **2023**, *62*, e202310733.
20. You, Q.; Wang, H.; Zhao, Y.; et al. Bottom-Up Construction of Metal–Organic Framework Loricae on Metal Nanoclusters with Consecutive Single Nonmetal Atom Tuning for Tailored Catalysis. *J. Am. Chem. Soc*. **2024**, *146*, 9026–9035.
21. Liu, H.-X.; Wang, W.-W.; Fu, X.-P.; et al. Direct cleavage of C=O double bond in CO_2 by the subnano MoO_x surface on Mo_2N. *Nat. Commun*. **2024**, *15*, 9126.
22. Yang, T.; Dong, Y.; Liu, C.; et al. Supramolecules Containing Homogeneous Electron-rich Cu Sites for Photocatalytic CO_2 Reduction to C_2H_6. *Adv. Funct. Mater*. **2025**, *35*, 2422348.
23. Lin, Z.; Yang, Z.; Wang, J.; et al. Unlocking the Potential of Oxide-Based Catalysts for CO_2 Photo-Hydrogenation: Oxygen Vacancies Promoted C–O Bond Cleavage in Key Intermediates. *Adv. Mater*. **2025**, *37*, 2408906.
24. Wu, J.; Liu, Z.; Lin, X.; et al. Breaking through water-splitting bottlenecks over carbon nitride with fluorination. *Nat. Commun*. **2022**, *13*, 6999.
25. Huo, Y.; Zhang, P.; Chi, J.; et al. Surface Functionalization and Defect Construction of SnO_2 with Amine Group for Enhanced Visible-Light-Driven Photocatalytic CO_2 Reduction. *Adv. Energy Mater*. **2024**, *14*, 2304282.
26. Li, W.; Zuo, G.; Ma, S.; et al. Localized photothermal effect mediated hollow S-scheme $NiCo_2O_4$@$ZnIn_2S_4$ for enhanced photocatalytic hydrogen evolution. *Appl. Catal. B Environ*. **2025**, *365*, 124971.
27. Wang, S.; Wang, J.; Wang, Y.; et al. Insight into the Selectivity-Determining Step of Various Photocatalytic CO_2 Reduction Products by Inorganic Semiconductors. *ACS Catal*. **2024**, *14*, 10760–10788.
28. Sun, Q.; Liu, X.; Gu, Q.; et al. Breaking the Conversion-Selectivity Trade-Off in Methanol Synthesis from CO_2 Using Dual Intimate Oxide/Metal Interfaces. *J. Am. Chem. Soc*. **2024**, *146*, 28885–28894.
29. Tang, J.; Guo, C.; Wang, T.; et al. A review of g‐C_3N_4‐based photocatalytic materials for photocatalytic CO_2 reduction. *Carbon Neutralizat.* **2024**, *3*, 557–583.
30. Anemüller, R.; Belden, K.; Brause, B.; et al. Hip and Knee Section, Treatment, Antimicrobials: Proceedings of International Consensus on Orthopedic Infections. *J. Arthroplast.* **2019**, *34*, S477–S482.
31. Sun, K.; Qian, Y.; Jiang, H.-L. Metal-Organic Frameworks for Photocatalytic Water Splitting and CO_2 Reduction. *Angew. Chem. Int. Ed*. **2023**, *62*, e202217565.
32. Feng, J.; Chen, S.; Lu, Z.; et al. Metal-Organic Frameworks for Photocatalytic CO_2 Reduction: Progress and Prospects. *ACS Appl. Mater. Interfaces* **2025**, *17*, 60028–60054.

33. Mohata, S.; Majumder, P.; Banerjee, R. Design and structure-function interplay in covalent organic frameworks for photocatalytic CO_2 reduction. *Chem. Soc. Rev*. **2025**, *54*, 6062–6087.
34. Qin, L.; Ma, C.; Zhang, J.; et al. Structural Motifs in Covalent Organic Frameworks for Photocatalysis. *Adv. Funct. Mater*. **2024**, *34*, 2401562.
35. Li, B.; Liu, X.-J.; Zhu, H.-W.; et al. A Review on Bi_2WO_6-Based Materials for Photocatalytic CO_2 Reduction. *Small* **2024**, *20*, 2406074.
36. Kaur, J.; Peter, S.C. Two-Dimensional Perovskites for Photocatalytic CO_2 Reduction. *Angew. Chem. Int. Ed*. **2025**, *64*, e202418708.
37. Zheng, M.; Zhang, J.; Wang, P.; et al. Recent Advances in Electrocatalytic Hydrogenation Reactions on Copper-Based Catalysts. *Adv. Mater.* **2024**, *36*, 2307913.
38. de Almeida, J.C.; Wang, Y.; Rodrigues, T.A.; et al. Copper-based Materials for Photo and Electrocatalytic Process: Advancing Renewable Energy and Environmental Applications. *Adv. Funct. Mater.* **2025**, 2502901. https://doi.org/10.1002/adfm.202502901.
39. Liu, L.; Wang, Z.; Zhang, J.; et al. Tunable Interfacial Charge Transfer in a 2D-2D Composite for Efficient Visible-Light-Driven CO_2 Conversion. *Adv. Mater.* **2023**, *35*, 2300643.
40. Feng, C.; Hu, M.; Zuo, S.; et al. Ru-OV Site-Mediated Product Selectivity Switch for Overall Photocatalytic CO_2 Reduction. *Adv. Mater.* **2025**, *37*, 2411813.
41. Li, B.; Zhang, X.; Chen, M.; et al. Multichannel charge transfer mediated by polyoxometalate loaded SnS_2 wrapped Te nanostructures for efficient photocatalytic CO_2 reduction. *Appl. Catal. B Environ.* **2025**, *377*, 125509.
42. Li, M.; Han, Z.; Hu, Q.; et al. Recent progress in solar-driven CO_2 reduction to multicarbon products. *Chem. Soc. Rev*. **2024**, *53*, 9964–9975.
43. Zhu, H.-W.; Guo, R.-T.; Liu, C.; et al. Recent progress on photocatalytic reduction of CO_2 to C_{2+} products. *J. Mater. Chem. A* **2024**, *12*, 21677–21703.
44. Chen, H.; Zhao, C.; Chen, X. Photocatalytic Reduction of Carbon Dioxide: Designing the Active Sites and Tracking the Pathways. *Chem. Asian J*. **2025**, *20*, e202500106.
45. Chen, G.; Gao, R.; Zhao, Y.; et al. Alumina-Supported CoFe Alloy Catalysts Derived from Layered-Double-Hydroxide Nanosheets for Efficient Photothermal CO_2 Hydrogenation to Hydrocarbons. *Adv. Mater.* **2018**, *30*, 1704663.
46. Wu, Y.; Hu, Q.; Chen, Q.; et al. Fundamentals and Challenges of Engineering Charge Polarized Active Sites for CO_2 Photoreduction toward C_2 Products. *Acc. Chem. Res.* **2023**, *56*, 2500–2513.
47. Li, X.; Yu, J.; Jaroniec, M.; et al. Cocatalysts for Selective Photoreduction of CO_2 into Solar Fuels. *Chem. Rev*. **2019**, *119*, 3962–4179.
48. Che, W.; Zhao, S.; Byun, W.J.; et al. From Carbon Nitrides to COFs: Opportunities and Prospects in Photocatalytic CO_2 Reduction. *Adv. Mater*. **2025**, *37*, 2306961.
49. Yang, J.; Deng, C.; Lei, Y.; et al. Fe–N Co-Doped $BiVO_4$ Photoanode with Record Photocurrent for Water Oxidation. *Angew. Chem. Int. Ed*. **2025**, *64*, e202416340.
50. Huang, T.; Han, J.; Li, Z.; et al. Unraveling the Essential Role of Consecutive Protonation Steps in Photocatalytic CO_2 Reduction when Using Au Nanorods in a MOF. *Angew. Chem. Int. Ed*. **2025**, *64*, e202500269.
51. Lin, Z.; Yu, X.; Zhao, Z.; et al. Controlling crystallization in covalent organic frameworks to facilitate photocatalytic hydrogen production. *Nat. Commun*. **2025**, *16*, 1940.
52. Feng, J.; Zhang, L.; Liu, S.; et al. Modulating adsorbed hydrogen drives electrochemical CO_2-to-C_2 products. *Nat. Commun.* **2023**, *14*, 4615.
53. Feng, C.; Wang, F.; Liu, Z.; et al. A self-healing catalyst for electrocatalytic and photoelectrochemical oxygen evolution in highly alkaline conditions. *Nat. Commun.* **2021**, *12*, 5980.
54. Fu, H.; Lei, Y.; Zhang, Q.; et al. Optimization of CO_2 Mass Transfer and Modulation of Reaction Kinetics for Efficient CO_2 Conversion via a Three-Phase Photocatalytic Flow System. *Adv. Funct. Mater*. **2025**, e15361. https://doi.org/10.1002/adfm.202515361.
55. Alvarez, I.B.; Le, T.; Hosseini, H.; et al. Bond Selective Photochemistry at Metal Nanoparticle Surfaces: CO Desorption from Pt and Pd. *J. Am. Chem. Soc*. **2024**, *146*, 12431–12443.
56. Liu, B.; Hu, Z.; Li, Y.; et al. Simultaneous value-added utilization of photogenerated electrons and holes on Pd/TiO_2. *Nat. Commun*. **2025**, *16*, 6014.
57. Ru, Q.; Zhang, B.; Li, S.; et al. Overcoming the bottleneck in one-electron reduction of CO_2 with mechanical energy-driven triboelectric plasma-enabled catalysis. *Chem. Eng. J.* **2025**, *519*, 165012.
58. Li, L.; Liu, W.; Shi, T.; et al. Photoexcited Single-Electron Transfer for Efficient Green Synthesis of Cyclic Carbonate from CO_2. ACS Mater. Lett. **2023**, *5*, 1219–1226.
59. Xu, Z.; Lu, R.; Lin, Z.-Y.; et al. Electroreduction of CO_2 to methane with triazole molecular catalysts. *Nat. Energy.* **2024**, *9*, 1397–1406.

60. Bains, A.K.; Sau, A.; Portela, B.S.; et al. Efficient super-reducing organic photoredox catalysis with proton-coupled electron transfer mitigated back electron transfer. *Science.* **2025**, *388*, 1294–1300.
61. Wang, W.; Deng, C.; Xie, S.; et al. Photocatalytic C–C Coupling from Carbon Dioxide Reduction on Copper Oxide with Mixed-Valence Copper(I)/Copper(II). *J. Am. Chem. Soc.* **2021**, *143*, 2984–2993.
62. Li, Y.; Chen, Y.; Wang, Q.; et al. Realizing C–C Coupling via Accumulation of C_1 Intermediates within Dual-Vacancy-Induced Dipole-Limited Domain Field to Propel Photoreduction of CO_2-to-C_2 Fuel. *Adv. Mater*. **2025**, *37*, 2414994.
63. Ding, J.; Du, P.; Li, P.; et al. Highly Active Photoreduction of Atmospheric-Concentration CO_2 into CH_3COOH over Palladium Particles on Nb_2O_5 Nanosheets. *Angew. Chem. Int. Ed*. **2025**, *64*, e202414453.
64. Shi, X.; Dai, W.; Li, X.; et al. Lattice-Matched S-Scheme High-Entropy Oxide Heterojunction for Efficient Visible-Light-Driven CO_2 Photomethanation. *Adv. Funct. Mater.* **2025**, e11696. https://doi.org/10.1002/adfm.202511696.
65. Li, X.; Li, L.; Liu, X.; et al. Designing multi-metal-site nanosheet catalysts for CO_2 photoreduction to ethylene. *Nat. Commun.* **2025**, *16*, 6500.
66. Li, W.; Zhang, Y.; Wang, Y.; et al. Graphdiyne facilitates photocatalytic CO_2 hydrogenation into C_{2+} hydrocarbons. *Appl. Catal. B Environ*. **2024**, *340*, 123267.
67. Liang, M.; Shao, X.; Choi, J.Y.; et al. Modified TiO_2/In_2O_3 heterojunction with efficient charge separation for visible-light-driven photocatalytic CO_2 reduction to C_2 product. *J. Energy Chem*. **2024**, *98*, 714–720.
68. Zhang, Y.; Li, W.; Tian, F.; et al. Construction of multiple channels for electron transport in In_2S_3/In_2O_3/rGO heterojunctions to boost photocatalytic CO_2 conversion to C_{2+} hydrocarbons. *Chem. Eng. J.* **2023**, *477*, 147129.
69. Du, P.; Ding, J.; Liu, C.; et al. Interface-Engineering-Induced C–C Coupling for C_2H_4 Photosynthesis from Atmospheric-Concentration CO_2 Reduction. *Angew. Chem. Int. Ed*. **2025**, *64*, e202421353.
70. Hao, S.; Chen, Y.; Peng, C.; et al. Photocatalytic Coupling of CH_4 and CO_2 to Ethanol on Asymmetric Ce–O–Zn Sites. *Adv. Funct. Mater*. **2024**, *34*, 2314118.
71. Subrahmanyam, M.; Kaneco, S.; Alonso-Vante, N. A screening for the photo reduction of carbon dioxide supported on metal oxide catalysts for C_1–C_3 selectivity. *Appl. Catal. B Environ.* **1999**, *23*, 169–174.
72. Wang, J.; Lin, S.; Tian, N.; et al. Nanostructured Metal Sulfides: Classification, Modification Strategy, and Solar-Driven CO_2 Reduction Application. *Adv. Funct. Mater*. **2021**, *31*, 2008008.
73. Liu, C.; Xiao, Y.; Wan, W.; et al. Different behaviors on the external and inner surface of hollow CdS/VS-MoS_2 heterojunctions in photoelectrocatalytic CO_2 reduction via SH-assisted mechanism. *Appl. Catal. B Environ.* **2023**, *325*, 122394.
74. Wang, B.; Jiang, Z.; Yu, J.C.; et al. Enhanced CO_2 reduction and valuable C_{2+} chemical production by a CdS-photosynthetic hybrid system. *Nanoscale* **2019**, *11*, 9296–9301.
75. Yang, X.; Lan, X.; Zhang, Y.; et al. Rational design of MoS_2@COF hybrid composites promoting C–C coupling for photocatalytic CO_2 reduction to ethane. *Appl. Catal. B Environ*. **2023**, *325*, 122393.
76. Liu, Y.; Liu, Y.; Luo, G.; et al. Photothermally inducing SnS_2 phase transition in Cu_2O@CuS@SnS_2 core—Shell heterostructure to trigger efficient photocatalytic CO_2 reduction. *Chem. Eng. J.* **2025**, *510*, 161537.
77. Zhang, J.; Duan, L.; Zhang, W.; et al. Crystal-Facet Engineering of Mesoporous CuS Cascade Nanoreactors Enhances Photocatalytic C–C Coupling of CO_2-to-C_2H_4. *Angew. Chem. Int. Ed.* **2025**, *64*, e202423861.
78. Huang, H.B.; Zhang, N.; Xu, J.Y.; et al. Photocatalytic CO_2-to-Ethylene Conversion over Bi_2S_3/CdS Heterostructures Constructed via Facile Cation Exchange. *Research* **2022**, *2022*, 9805879.
79. Ren, L.; Yang, X.; Sun, X.; et al. Cascaded *CO–*COH Intermediates on a Nonmetallic Plasmonic Photocatalyst for CO_2-to-C_2H_6 with 90.6% Selectivity. *Angew. Chem. Int. Ed*. **2024**, *63*, e202404660.
80. Wang, J.; Zhang, H.; Mu, N.; et al. Sulfur in multiple chemical states synergistic bimetallic sites on $CuIn_{11}S_{17}$ promoting photocatalytic evolution of C_2H_4 from CO_2. *Appl. Catal. B Environ*. **2025**, *377*, 125480.
81. Lv, L.; Liu, Y.; Li, X.; et al. Synergistic Engineering of Zinc Vacancies and Er-Doping in $ZnIn_2S_4$ Nanosheets for Enhanced CO_2 Photoreduction via Optimized Charge Dynamics. *Carbon Neutralization* **2025**, *4*, e70021.
82. Song, W.; Wang, C.; Liu, Y.; et al. Unlocking Copper-Free Interfacial Asymmetric C–C Coupling for Ethylene Photosynthesis from CO_2 and H_2O. *J. Am. Chem. Soc*. **2024**, *146*, 29028–29039.
83. Zheng, X.; Song, Y.; Gao, Q.; et al. Controllable-Photocorrosion Balance Endows ZnCdS Stable Photocatalytic Hydrogen Evolution. *Adv. Funct. Mater*. **2025**, *35*, 2506159.
84. Shi, H.; Liang, Y.; Hou, J.; et al. Boosting Solar-Driven CO_2 Conversion to Ethanol via Single-Atom Catalyst with Defected Low-Coordination Cu-N_2 Motif. *Angew. Chem. Int. Ed*. **2024**, *63*, e202404884.
85. Wang, Q.; He, M.Q.; Yang, P.X.; et al. Selective Photocatalytic Conversion of CO_2 to Ethanol via Unsaturated Cu-O Domains. *ACS Nano* **2024**, *18*, 33576–33586.
86. Zeng, D.; Wang, H.; Zhu, X.; et al. Photocatalytic conversion of CO_2 to acetic acid by CuPt/WO_3: Chloride enhanced C-C coupling mechanism. *Appl. Catal. B Environ*. **2023**, *323*, 122177.

87. Zhang, P.; Li, N.; Li, L.; et al. g-C_3N_4-Based Photocatalytic Materials for Converting CO_2 into Energy: A Review. *Chemphyschem* **2024**, *25*, e202400075.
88. Sun, Z.; Wang, H.; Wu, Z.; et al. g-C_3N_4 based composite photocatalysts for photocatalytic CO2 reduction. Catal. *Today* **2018**, *300*, 160–172.
89. Xu, Y.; Gao, S.-P. Band gap of C_3N_4 in the GW approximation. *Int. J. Hydrog. Energy* **2012**, *37*, 11072–11080.
90. Huang, Z.; Chen, H.; Zhao, L.; et al. Constructing g-C_3N_4quantum dots modified g-C_3N_4/GO nanosheet aerogel for UV-Vis-NIR driven highly efficient photocatalytic H_2 production. *Int. J. Hydrog. Energy* **2019**, *44*, 31041–31052.
91. Mo, Z.; Zhu, X.; Jiang, Z.; et al. Porous nitrogen-rich g-C_3N_4 nanotubes for efficient photocatalytic CO_2 reduction. *Appl. Catal. B Environ.* **2019**, *256*, 117854.
92. Li, X.; Xiong, J.; Gao, X.; et al. Recent advances in 3D g-C_3N_4 composite photocatalysts for photocatalytic water splitting, degradation of pollutants and CO_2 reduction. *J. Alloys Compd*. **2019**, *802*, 196–209.
93. Chen, H.L.; Liu, F.Y.; Lin, Y.Y.; et al. Photocatalytic CO_2 reduction to C_1–C_5 hydrocarbons using $K_2Fe_2O_4$/g-C_3N_4 as coupling photocatalyst. *Mater. Today Sustain*. **2023**, *23*, 100430.
94. Chen, Z.; Ding, G.; Wang, Z.; et al. Precision Molecular Engineering of Carbon Nitride for Efficient and Selective Photoreduction of CO_2 to C_2H_6 in Pure Water. *Adv. Funct. Mater*. **2025**, *35*, 2423213.
95. Gao, Q.; Qi, W.; Li, Y.; et al. Regulating Local Electron Density of Cyano Sites in Graphitic Nitride Carbon by Giant Internal Electric Field for Efficient CO_2 Photoreduction to Hydrocarbons. *Small* **2024**, *20*, 2404822.
96. Niu, P.; Yang, Y.; Yu, J.C.; et al. Switching the selectivity of the photoreduction reaction of carbon dioxide by controlling the band structure of a g-C_3N_4 photocatalyst. *Chem. Commun*. **2014**, *50*, 10837–10840.
97. Andrei, V.; Roh, I.; Lin, J.-A.; et al. Perovskite-driven solar C_2 hydrocarbon synthesis from CO_2. *Nat. Catal*. **2025**, *8*, 137–146.
98. Rowsell, J.L.C.; Yaghi, O.M. Metal-organic frameworks: A new class of porous materials. *Microporous Mesoporous Mater.* **2004**, *73*, 3–14.
99. Wang, W.W.; Song, S.J.; Wang, P.; et al. Chemical Bonding of g-C_3N_4/UiO-66(Zr/Ce) from Zr and Ce Single Atoms for Efficient Photocatalytic Reduction of CO_2 under Visible Light. *ACS Catal.* **2023**, *13*, 4597–4610.
100. Zhao, B.; Qiu, X.; Song, Y.; et al. Regulating Asymmetric Charge Distribution in Cu_2MoS_4 Nanosheets for Enhanced Photocatalytic CO_2 Reduction. *Small* **2025**, *21*, 2500877.
101. Zhou, Q.; Guo, Y.; Zhu, Y. Reticular copper dual sites embedded with semiconductor particles for selective CO_2-to-C_2H_4 photoreduction. *Nat. Catal*. **2025**, *8*, 728–739.
102. Xie, S.; Li, Y.; Sheng, B.; et al. Self-reconstruction of paddle-wheel copper-node to facilitate the photocatalytic CO_2 reduction to ethane. *Appl. Catal. B Environ*. **2022**, *310*, 121320.
103. Chen, D.; Chu, B.; Li, F.; et al. Synergistic Catalysis by Cu Single Atoms and Atomically Cu-Doped Au Nanoparticles in a Metal—Organic Framework for Photocatalytic CO_2 Reduction to C_2H_6. *J. Am. Chem. Soc*. **2025**, *147*, 22705–22713.
104. Huang, Z.-W.; Hu, K.-Q.; Li, X.-B.; et al. Thermally Induced Orderly Alignment of Porphyrin Photoactive Motifs in Metal—Organic Frameworks for Boosting Photocatalytic CO_2 Reduction. *J. Am. Chem. Soc*. **2023**, *145*, 18148–18159.
105. Mishra, B.; Alam, A.; Chakraborty, A.; et al. Covalent Organic Frameworks for Photocatalysis. *Adv. Mater.* **2024**, 2413118. https://doi.org/10.1002/adma.202413118.
106. Hirani, Z.; Schweitzer, N.M.; Vitaku, E.; et al. A Phenazine-Based Two-Dimensional Covalent Organic Framework for Photochemical CO_2 Reduction with Increased Selectivity for Two-Carbon Products. *Angew. Chem. Int. Ed*. **2025**, *64*, e202502799.
107. Liu, Q.; Li, Q.; Li, Y.; et al. Two-Dimensional Covalent Organic Frameworks in Organic Electronics. *Angew. Chem. Int. Ed*. **2025**, *64*, e202502536.
108. Hsueh, C.-H.; He, C.; Zhang, J.; et al. Three-Dimensional Mesoporous Covalent Organic Framework for Photocatalytic Oxidative Dehydrogenation to Quinoline. *J. Am. Chem. Soc*. **2024**, *146*, 33857–33864.
109. Zhu, J.; Huang, L.; Dong, W.; et al. Enantioselective Rhodium-Catalyzed Addition of Arylboroxines to N-Unprotected Ketimines: Efficient Synthesis of Cipargamin. *Angew. Chem. Int. Ed*. **2019**, *58*, 16119–16123.
110. Yang, J.; Chen, Z.; Zhang, L.; et al. Covalent Organic Frameworks for Photocatalytic Reduction of Carbon Dioxide: A Review. *ACS Nano* **2024**, *18*, 21804–21835.
111. Guan, G.-W.; Zheng, S.-T.; Zhang, L.-P.; et al. Regulating Charge Distribution in Porphyrin-Based Polymer for Achieving Photocatalytic CO2 Conversion to CH_4 or C_2H_6. *Small* **2025**, *21*, 2409575.
112. Chen, X.; Liu, C.; Yang, T.; et al. Cu atom pairs within covalent organic frameworks facilitate the photocatalytic reduction of CO_2 to C_2H_6. *Appl. Catal. B Environ*. **2025**, *377*, 125499.
113. Hu, Y.; Liu, G.; Song, T.; et al. Single-atom Cu sites on covalent organic frameworks with Kagome lattices for visible-light-driven CO_2 reduction to propylene. *Appl. Catal. B Environ*. **2025**, *361*, 124587.

114. Wang, Y.-C.; Shi, W.-J.; Zhang, J.-H.; et al. Rapid electron transfer via imine-linked interface in dinuclear cobalt MOF@COF Z-scheme heterojunction for enhanced photocatalytic CO_2 reduction with H_2O. *Chem. Eng. J*. **2025**, *517*, 164327.
115. Zhang, W.; Zhong, Z.; Wei, X.; et al. Single-Crystal Metal—Organic and Covalent Organic Framework Hybrids Enable Efficient Photoelectrochemical CO_2 Reduction to Ethanol. *J. Am. Chem. Soc*. **2025**, *147*, 17975–17984.
116. Huang, Y.; Du, P.; Shi, W.-X.; et al. Filling COFs with bimetallic nanoclusters for CO_2-to-alcohols conversion with H_2O oxidation. *Appl. Catal. B Environ*. **2021**, *288*, 120001.
117. Zhang, Y.; Guan, X.; Meng, Z.; et al. Supramolecularly Built Local Electric Field Microenvironment around Cobalt Phthalocyanine in Covalent Organic Frameworks for Enhanced Photocatalysis. *J. Am. Chem. Soc.* **2025**, *147*, 3776–3785.
118. Zheng, Y.; Yang, J.; Qiao, Z.-A. Condensed Matter Chemistry: The Defect Engineering of Porous Materials. *Prog. Chem*. **2023**, *35*, 954–967.
119. Zhang, M.; Zhang, D.; Jing, X.; et al. Engineering NH_2-Cu-NH_2 Triple-atom Sites in Defective MOFs for Selective Overall Photoreduction of CO_2 into CH_3COCH_3. *Angew. Chem. Int. Ed*. **2024**, *63*, e202402755.
120. Zhang, L.; Liu, T.; Liu, T.; et al. Improving photocatalytic performance of defective titania for carbon dioxide photoreduction by Cu cocatalyst with SCN-ion modification. *Chem. Eng. J.* **2023**, *463*, 142358.
121. Wang, J.; Yang, C.; Mao, L.; et al. Regulating the Metallic Cu–Ga Bond by S Vacancy for Improved Photocatalytic CO_2 Reduction to C_2H_4. *Adv. Funct. Mater*. **2023**, *33*, 2213901.
122. Chen, H.; Wang, L.; Long, D.; et al. Advancing the ethanol pathway during the competitive photocatalytic CO_2 reduction in a defective transition metal dichalcogenide. *Appl. Catal. B Environ*. **2024**, *357*, 124260.
123. Liu, B.; Cheng, M.; Zhang, C.; et al. Au-Cu dual-single-atom sites on Bi_2WO_6 with oxygen vacancy for CO_2 photoreduction towards multicarbon products. *Appl. Catal. B Environ*. **2024**, *357*, 124263.
124. Das, K.; Chakraborty, S.; Kediya, S.; et al. Dopant and Exfoliation Induced Simultaneous Modification of Charge Density and C–C Coupling Sites for Efficient CO_2 Photoreduction to Ethylene. *Angew. Chem. Int. Ed.* **2025**, *64*, e202423471.
125. Xing, F.; Li, Q.; Li, J.; et al. Cu doping induced asymmetric Cu-Vs-In active sites in In_2S_3 for efficient photocatalytic C_2H_4 conversion from CO_2. *J. Colloid Interface Sci*. **2025**, *691*, 137388.
126. Gao, S.; Guan, H.; Wang, H.; et al. Creation of $Sn_xNb_{1-x}O_2$ solid solution through heavy Nb-doping in SnO_2 to boost its photocatalytic CO_2 reduction to C_{2+} products under simulated solar illumination. *J. Adv. Ceram*. **2022**, *11*, 1404–1416.
127. Shao, W.; Li, X.; Zhu, J.; et al. $Metal^{n+}$-$Metal^{\delta+}$ pair sites steer C-C coupling for selective CO_2 photoreduction to C_2 hydrocarbons. *Nano Res*. **2022**, *15*, 1882–1891.
128. Ni, B.; Zhang, G.; Wang, H.; et al. Correlating Oxidation State and Surface Ligand Motifs with the Selectivity of CO_2 Photoreduction to C_2 Products. *Angew. Chem. Int. Ed.* **2023**, *62*, e202215574.
129. Wu, Y.; Chen, Q.; Zhu, J.; et al. Selective CO_2-to-C_2H_4 Photoconversion Enabled by Oxygen-Mediated Triatomic Sites in Partially Oxidized Bimetallic Sulfide. *Angew. Chem. Int. Ed.* **2023**, *62*, e202301075.
130. Xu, M.; Zhang, Q.; Wei, S.; et al. Engineering Heteronuclear Dual-Metal Active Sites in Ordered Macroporous Architectures for Enhanced C_2H_4 Production from CO_2 Photoreduction. *Angew. Chem. Int. Ed*. **2025**, *64*, e202506072.
131. Zhang, Y.; Wei, T.; Ding, D.; et al. Aggregation-Induced Equidistant Dual Pt Atom Pairs for Effective CO_2 Photoreduction to C_2H_4. *ACS Catal*. **2025**, *15*, 5614–5622.
132. Wang, Y.; Jiang, J.; Yao, N.; et al. Enhanced photocatalytic CO_2 conversion over 0D/2D $AgVO_3/TiO_2$ heterojunctions assisted by Z-scheme charge separation. *Sci. China Mater*. **2024**, *67*, 1820–1829.
133. He, Q.; Ma, D.; Du, Y.; et al. An Atypical Heterojunction in Favor of Conversion of CO_2 and Sunlight into C_2H_4. *Adv. Sci*. **2025**, *12*, 2503336.
134. Zhang, Z.; Hu, Q.; Xie, J.; et al. CO_2 Photoreduction into C_2 Fuels Steered by Heteroatom Pair Sites in MxOy@Bi_2S_3 Heterojunction. *ACS Catal.* **2025**, *15*, 14021–14028.
135. Wu, Y.; Li, Z.; Chen, Q.; et al. Cooperative Atomic Palladium Site and Island-Distributed S-Scheme Heterostructure for Photocatalytic C_2H_6 Production. *ACS Catal.* **2025**, *15*, 3558–3569.
136. Yu, S.; Wilson, A.J.; Heo, J.; et al. Plasmonic Control of Multi-Electron Transfer and C–C Coupling in Visible-Light-Driven CO_2 Reduction on Au Nanoparticles. *Nano Lett*. **2018**, *18*, 2189–2194.
137. Li, N.; Jiang, R.; Li, Y.; et al. Plasma-Assisted Photocatalysis of CH_4 and CO_2 into Ethylene. *ACS Sustain. Chem. Eng*. **2019**, *7*, 11455–11463.
138. Devasia, D.; Wilson, A.J.; Heo, J.; et al. A rich catalog of C–C bonded species formed in CO_2 reduction on a plasmonic photocatalyst. *Nat. Commun*. **2021**, *12*, 2612.
139. Lu, C.; Li, J.; Yan, J.; et al. Surface plasmon resonance and defects on tungsten oxides synergistically boost high-selective CO_2 reduction for ethylene. *Appl. Mater. Today* **2020**, *20*, 100744.
140. Yang, X.; Ren, L.; Chen, Z.; et al. Constructing an Active Sulfur-Vacancy-Rich Surface for Selective *CH_3-CH_3 Coupling in CO_2-to-C_2H_6 Conversion With 92% Selectivity. *Adv. Mater*. **2025**, *37*, 2412299.

141. Xie, Z.; Cheng, W.; Luo, H.; et al. Artificial Photothermal Synthesis of Hydrocarbons from CO_2 and H_2O. *Adv. Energy Mater*. **2025**, 2501840. https://doi.org/10.1002/aenm.202501840.
142. He, H.; Ren, Y.; Zhu, Y.-H.; et al. Continuous Flow Photothermal Catalytic CO_2 Reduction: Materials, Mechanisms, and System Design. *ACS Catal*. **2025**, *15*, 10480–10520.
143. Song, H.; Sun, K.; Huang, H.; et al. Integrating photochemical and photothermal effects for selective oxidative coupling of methane into C_{2+} hydrocarbons with multiple active sites. *Nat. Commun*. **2025**, *16*, 2831.
144. Feng, G.; Wang, S.; Li, S.; et al. Highly Selective Photoelectroreduction of Carbon Dioxide to Ethanol over Graphene/Silicon Carbide Composites. *Angew. Chem. Int. Ed*. **2023**, *62*, e202218664.
145. Yan, K.; Wu, D.; Wang, T.; et al. Highly Selective Ethylene Production from Solar-Driven CO_2 Reduction on the Bi_2S_3@In_2S_3 Catalyst with In–SV–Bi Active Sites. *ACS Catal*. **2023**, *13*, 2302–2312.
146. Li, X.; Li, L.; Chu, X.; et al. Photothermal CO_2 conversion to ethanol through photothermal heterojunction-nanosheet arrays. *Nat. Commun*. **2024**, *15*, 5639.
147. Peng, R.; Ren, Y.; Si, Y.; et al. Strong Photothermal Tandem Catalysis for CO_2 Reduction to C_2H_4 Boosted by Zr–O–W Interfacial H_2O Dissociation. *ACS Catal*. **2025**, *15*, 1–13.
148. Yu, M.; Li, M.; Zhang, X.; et al. Coupling Photocatalytic Reduction and Biosynthesis Towards Sustainable CO_2 Upcycling. *Angew. Chem. Int. Ed*. **2025**, *64*, e202423995.
149. Cai, Y.; Yang, R.; Fu, J.; et al. Self-pressurizing nanoscale capsule catalysts for CO_2 electroreduction to acetate or propanol. *Nat. Synth*. **2024**, *3*, 891–902.
150. Du, H.; Liu, L.-X.; Li, P.; et al. Enriching reaction intermediates in multishell structured copper catalysts for boosted propanol electrosynthesis from carbon monoxide. *ACS Nano* **2023**, *17*, 8663–8670.
151. Zhu, W.; Zhang, Y.-J.; Zhang, H.; et al. Active and selective conversion of CO_2 to CO on ultrathin Au nanowires. *J. Am. Chem. Soc*. **2014**, *136*, 16132–16135.
152. Zhu, W.; Michalsky, R.; Metin, Ö.; et al. Monodisperse Au nanoparticles for selective electrocatalytic reduction of CO_2 to CO. *J. Am. Chem. Soc*. **2013**, *135*, 16833–16836.
153. Xie, L.; Cai, Y.; Jiang, Y.; et al. Direct low concentration CO_2 electroreduction to multicarbon products via rate-determining step tuning. *Nat. Commun.* **2024**, *15*, 10386.
154. Uthirakumar, P.; Son, H.; Dao, V.; et al. Accelerating photoelectrochemical CO_2RR selectively of C_{2+} products by integrating Ag/Pd cocatalysts on Cu/Cu_2O/CuO heterojunction nanorods. *J. Environ. Chem. Eng*. **2024**, *12*, 112442.
155. Guo, X.; Wang, C.; Yang, Z.; et al. Boosting C_{2+} production from photoelectrochemical CO_2 reduction on gallium doped Cu_2O. *Chem. Eng. J*. **2023**, *471*, 144539.
156. Chen, M.; Sun, Y.-H.; Zhou, D.; et al. Efficient CO_2 reduction to C_2 products in a Ce-TiO_2 photoanode-driven photoelectrocatalysis system using a Bnanometer Cu_2O cathode. *Appl. Catal.* A *Gen.* **2024**, *687*, 119966.
157. Liu, Q.; Bai, C.; Zhu, C.; et al. M/BiOCl-(M = Pt, Pd, and Au) Boosted Selective Photocatalytic CO_2 Reduction to C_2 Hydrocarbons via *CHO Intermediate Manipulation. *Adv. Sci*. **2024**, *11*, 2400934.
158. Jiang, Y.; Lv, C.; Lu, B.; et al. Ag Stabilized Cu^+/Cu^0 Interface Catalysts for Enhanced CO_2 Electroreduction to C_{2+} Products at Ampere Level Current Density. *ACS Nano* **2025**, *19*, 11263–11272.
159. Wei, Y.; Duan, R.; Zhang, Q.; et al. Photoelectrocatalytic reduction of CO_2 catalyzed by TiO_2/TiN nanotube heterojunction: Nitrogen assisted active hydrogen mechanism. *Chin. J. Catal.* **2023**, *47*, 243–253.
160. Zuo, L.; Deng, Y.; Chen, L.; et al. Fundamental Insights into Photoelectrochemical Carbon Dioxide Reduction: Elucidating the Reaction Pathways. *ACS Catal.* **2024**, *14*, 16795–16833.
161. Huang, Y.; Du, P.; Shi, W.-X.; et al. Filling COFs with bimetallic nanoclusters for CO_2-to-alcohols conversion with H_2O oxidation. *Appl. Catal. B Environ*. **2021**, *288*, 120001.
162. Yang, R.; Cai, Y.; Qi, Y.; et al. How local electric field regulates C–C coupling at a single nanocavity in electrocatalytic CO_2 reduction. *Nat. Commun.* **2024**, *15*, 7140.
163. Cai, Y.; Fu, J.; Zhou, Y.; et al. Insights on forming N,O-coordinated Cu single-atom catalysts for electrochemical reduction CO_2 to methane. *Nat. Commun.* **2021**, *12*, 586.
164. Zhuang, Z.; Wang, G.; Zhao, W.; et al. Silver-doped porous copper catalysts for efficient resource utilization of CO-containing flue gases. *ACS Environ. Au* **2025**, *5*, 287–297.
165. Ye, Z.; Shen, B.; Kang, D.; et al. A data-driven approach for the guided regulation of exposed facets in nanoparticles. *Nat. Synth.* **2024**, *3*, 922–929.
166. Su, L.; Rodríguez-Jiménez, S.; Short, M.I.M.; et al. Adapting gas fermenting bacteria for light-driven domino valorization of CO_2. *Chem. Sci*. **2025**, *16*, 11801–11808.
167. Wang, Q.; Kalathil, S.; Pornrungroj, C.; et al. Bacteria–photocatalyst sheet for sustainable carbon dioxide utilization. *Nat. Catal*. **2022**, *5*, 633–641.
168. Tian, Y.; Guo, Z.; He, J.; et al. Light-driven eosin Y-Ralstonia eutropha biohybrid for CO_2 conversion to acetoin via specific photo-induced electron transfer and metabolic engineering. *J. CO_2 Util.* **2025**, *93*, 103051.

169. Chen, N.; Xi, J.; He, T.; et al. Beyond natural synthesis via solar-decoupled biohybrid photosynthetic system. *Chem* **2025**, *11*, 102381.
170. Bai, X.; Li, Y.; Xie, Y.; et al. High-throughput screening of CO_2 cycloaddition MOF catalyst with an explainable machine learning model. *Green Energy Environ.* **2025**, *10*, 132–138.
171. Yang, Y.; Zhou, J.; Zhao, Z.; et al. Atomic-scale identification of active sites of oxygen reduction nanocatalysts. *Nat. Catal*. **2024**, *7*, 796–806.
172. Sun, M.Z.; Huang, B.L. Direct Machine Learning Predictions of C_3 Pathways. *Adv. Energy Mater*. **2024**, *14*, 2400152.
173. Li, J.; Wang, K.; Zhang, Y.; et al. Prediction of Carbon Dioxide Reduction Catalyst Using Machine Learning with a Few-Feature Model: WLEDZ. *J. Phys. Chem. C* **2022**, *126*, 18235–18244.